Journal of Science and Transport Technology
Journal homepage: https://jstt.vn/index.php/en

# Predicting the response of a Double-Story Single-Bay (DSSB) RC Frame through hybrid FEA-ANN

Afaq Ahmad[1], Hoa Thi Trinh[2,*], Ammar T. Al-Sayegh[3]
[1]OsloMet University, Norway. Email: afaq.ahmad@oslomet.no
[2]Advanced Materials and Intelligent Systems for Infrastructure and High-Speed Rail (AMIS-HSR) research group, University of Transport Technology, Hanoi, Vietnam. Email: hoatt85@utt.edu.vn
[3]Civil Engineering Department, Kuwait University. Email:al.sayegh@ku.edu.kw

**Article info**
**Type of article:**
Original research paper

**DOI:**
https://doi.org/10.58845/jstt.utt.2025.en.5.4.238-279

***Corresponding author:**
Email address:
hoatt85@utt.edu.vn

**Received:** 02/10/2025
**Received in Revised Form:** 25/11/2025
**Accepted:** 18/12/2025

**Abstract:** Predicting the brittle response of reinforced concrete (RC) frames remains an active research problem. Different industries and research tools predict brittle responses with varying accuracy and analysis times, due to their inherent limitations. Also, the sophisticated Finite Element Tools, i.e., (ABAQUS, ANSYS, and DIANA), require costly computational costs and deep knowledge of defining material compared to the industry tool (SAP 2000). An Artificial Neural Network Finite Element Analysis (ANN-FEA) method is proposed to address this issue without incurring additional computational costs. This ANN-FEA method is designed for the analysis and design of both new and existing RC structures, such as Double-story single-bay (DSSB) Frames. For this study, one experimental control model (ECM) frame with three additional finite element models (FEM) is examined. The additional FEM models have: (i) Half Diameter of Stirrups in the Beam (HDB), (ii) Half Diameter of Stirrups in both Beam and Columns (HDBC), and (iii) Double Spacing of Stirrups in Beam and Columns (DSBC), as compared to the experimental model. This assessment focused on measuring the influence of critical design parameters, such as transverse reinforcement ratio (ρt), on the load-carrying capacity of DSSB, especially in a brittle manner. The findings confirmed that all the new FEA models and ANN-FEA exhibited less lateral load than CM, with reductions of 4.45% for HDB, 13.8% for HDBC, and 5.2% for DSBC.

**Keywords:** RC Frames, DSSB, Hybrid FEA-ANN, Structural Analysis Tools, Artificial Neural Network.

## 1. Introduction

Since the mid-1950s, the construction boom of multi-story buildings has significantly expanded the roles and expertise required of structural engineers. These professionals are now tasked with ensuring the safety, durability, and cost-effectiveness of reinforced concrete (RC) multi-story structures [1-7]. Over the years, the field of structural engineering has introduced a variety of complex analytical methodologies to meet these demands [8-11]. Today, advanced tools are employed to design new structures in line with updated guidelines and to evaluate existing RC structures against contemporary standards [12-17]. This evolution has led to increasingly sophisticated and detailed analyses, requiring

greater computational resources and time investments. Current requirements emphasize the importance of utilizing tools that can provide accurate predictions, particularly regarding brittle failure modes [18-24].

Over recent decades, extensive efforts have been made to develop models that accurately predict the brittle response of RC frame elements. Such analysis tools are essential for (i) designing new RC structures, (ii) assessing old RC structures in line with current guidelines, (iii) evaluating the strength, safety, and integrity of damaged or deteriorated structures, (iv) addressing issues arising post-construction or due to changes in the use or function of existing structures, and (v) investigating the causes of structural failures or collapses [1-7].

To tackle the challenges faced in the construction industry, structural engineers must assess the performance and response of reinforced concrete (RC) structures under extreme loading conditions [8-11]. This evaluation involves examining the load-carrying capacity of RC structures, with a particular emphasis on their brittle behavior and the failure mechanisms that may lead to catastrophic collapse. Presently, engineers employ nonlinear analysis methods to explore the brittle characteristics of RC structures, which require complex calculations. Nonlinear finite element analysis (NLFEA) software packages, such as ABAQUS [8] and ADINA [9], are primarily used for research purposes. In contrast, industry-standard software tools like (i.e., SAP 2000 and ETABS) [11] are generally effective at predicting flexural failure modes; however, they often struggle with accurately forecasting shear (brittle) failure modes. Given that shear failures tend to be abrupt and catastrophic, occurring with little warning, it is crucial for structural analysis tools to predict these failure modes with precision [1-7]. Accurate predictions are essential for developing safe and cost-effective design solutions that uphold the structural integrity and resilience of RC frame structures. Inaccurate forecasts can result in unsafe designs by overestimating the load-carrying capacity and ductility of structural components.

In structural engineering practice, various standards such as ACI-318 [12], EC2 [13], JSCE [14], NZ [15], KBSC [16], and CSA [17], are commonly applied to assess the response of RC frames under lateral loads. These guidelines typically rely on truss models and strut-and-tie frameworks to represent RC behavior at the ULS, with analyses traditionally performed using sectional methodologies. While these code-based predictions tend to correspond well with experimental results for flexural strength, discrepancies in shear resistance have been observed. These discrepancies are mainly due to their empirical foundations, which are derived from regression-based interpretations of test data. In contrast, the CFP method [25] offers an alternative ULS prediction model by conceptualizing RC elements as arch-like structures post-cracking, diverging significantly from conventional code assumptions. For a more comprehensive analysis under intricate loading scenarios, NLFEA [26-36] is often employed in conjunction with physical testing, utilizing complex 3D modeling, material nonlinearities, and advanced failure mechanisms. Additionally, soft computing (SC) strategies have emerged as innovative tools for structural evaluation, distinguishing themselves from NLFEA by using data-driven, heuristic algorithms rather than strict mechanical formulations [37-46]. More recently, ANNs have gained traction as efficient substitutes for traditional NLFEA in tasks like structural performance evaluation, damage detection, and reliability analysis, offering faster computation with promising accuracy [47-55].

To address this challenge efficiently, we introduce an Artificial Neural Network Finite Element Analysis (ANN-FEA) approach [56,57], as depicted in Fig. 1, which aims to establish a novel, stable, and computationally efficient technique for accurately predicting the nonlinear response of RC structures. This innovative method is designed for

both research and real-world applications, enabling effective design optimization and comprehensive parametric investigations. By leveraging Artificial Neural Networks (ANNs), the approach reduces computational demands compared to conventional nonlinear finite element analysis (NLFEA). The ANN-FEA technique models the nonlinear behavior of individual RC elements, such as beams and columns, by integrating finite elements with ANNs to forecast brittle failure modes and their corresponding load capacities. Training datasets are compiled from experimental results on basic structural configurations, which are then used to train the ANN models. The model's predictions are evaluated against design code specifications and alternative assessment techniques, focusing on ULS behavior, and are further validated through selective NLFEA.

In these ANN-based finite element (ANN-FE) models [56,57], ANNs act as failure criteria in nonlinear static pushover analysis, ensuring accurate predictions of structural behavior. The method's reliability and objectivity are confirmed by comparing its results for RC frames under static loading with experimental data and numerical benchmarks. Additionally, the ANN-FE model's predictions are evaluated against outputs from commercial and research-oriented structural analysis software. During pushover analysis, ANNs determine the load capacity and failure mechanisms of individual RC members, such as beams and columns. The findings indicate that the ANN-FE approach delivers more precise ULS predictions for RC structures than industry-standard programs like ETABS and SAP 2000 [11], while also being significantly faster and less computationally intensive than advanced research tools such as ABAQUS [8]. This ANN-FEA technique [56,57], applies to both new and existing RC structures, including continuous beams, and serves as the core methodology of this research. The process involves three main stages: (1) database development from experimental and numerical studies, (2) ANN training to predict failure modes, and (3) validation against established analysis methods.

• Artificial Neural Network (ANN) models are developed for RC beams and columns, based on experimental databases in the first step. These models serve as failure criteria for predicting shear failure modes in individual RC members, including beams and columns, as established in the authors' previous work [57-64].

• The second step involves the primary feature of this method, which is the subdivision of the structure into segments. These segments extend between points of maximum bending moment and points of contra-flexure or between consecutive points of contra-flexure, analogous to supported beams, as illustrated in Fig. 1 [56,57]. The behavior of these segments has been thoroughly investigated experimentally. This investigation systematically reduces the number of shear links in key structural elements to evaluate the accuracy of these structural analysis packages in predicting the observed shift in failure mode from flexural to shear when the quantity of shear links is reduced beyond a critical threshold.

• In the third step, the developed ANN models are used as failure criteria during the nonlinear pushover analysis. The analysis process halts if the applied force exceeds the predicted capacity of the members.

During the pushover analysis, the ANN is invoked at each load increment to predict the shear capacity of individual RC members. Specifically, the ANN models predict the ultimate shear load ($V_u$) for beams and columns based on current internal forces and geometric/material parameters. The analysis procedure extracts internal forces (bending moment M, shear force V, and axial force N for columns) from each frame element at the current load step, normalizes these values along with member properties according to Eq. 4, and feeds them to the corresponding ANN model. If the demand (current internal forces) exceeds the ANN-predicted capacity, the analysis stops and records the failure mode and capacity. This stopping

criterion corresponds to the Ultimate Limit State (ULS), representing the point at which member capacity is exhausted rather than simulating post-peak behavior.

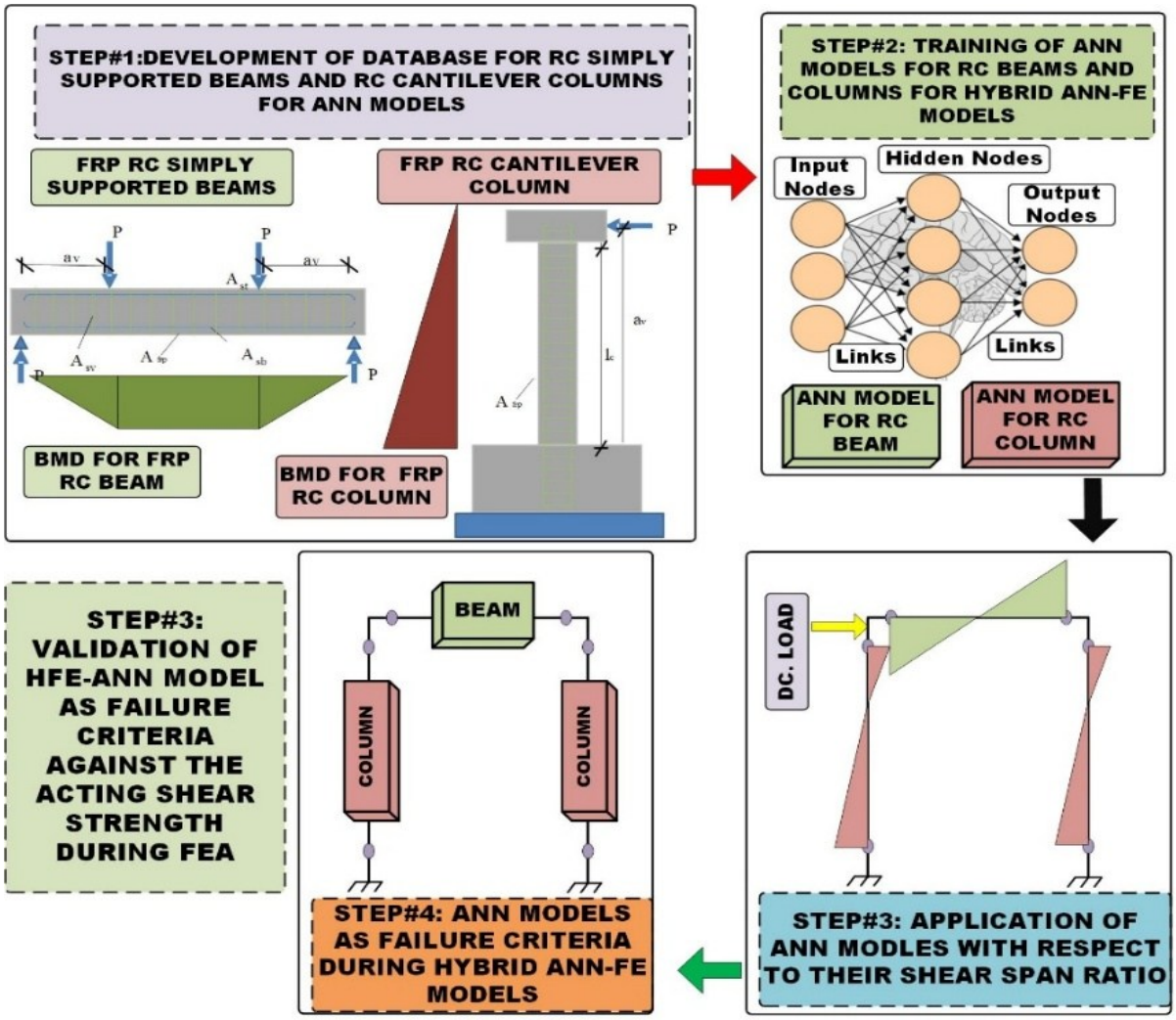


**Fig. 1**. Proposed Methodology of ANN-FEA for RC Frame [56,57]

• In the last step, for validation purposes, the ANN-FEA predictions are compared with the SAP2000 and ABAQUS predictions.

## 2. Novelty and contributions

The key novelty and contributions of this study can be summarized as follows: (1) Integration of ANN as a failure/limit criterion within pushover analysis, enabling accurate prediction of brittle failure modes; (2) Development of a segmentation strategy with ANN-calling mechanism for RC frame analysis; (3) Establishment of a comprehensive ANN-FEA coupling workflow that bridges member-level predictions to frame-level response; (4) Comparative assessment framework among ANN-FEA, ABAQUS, and SAP2000 for validation purposes; and (5) Application of the proposed methodology to the DSSB case study with systematic parametric investigation of transverse reinforcement effects.

The proposed ANN-FEA structural analysis method proves to be highly effective in designing new RC structures and assessing existing ones. Additionally, it enhances the capabilities of current professional structural analysis tools [56,57]. This ANN-FEA method is intended for the analysis and design of both new and existing RC structures. For this purpose, Emara et al [65] selected the double-story-single-bay (DSSB) RC frame as a case study for the numerical investigation of the effect of detailing on the frame's capacity. After calibration, the peak lateral load and peak displacement values

of the FEA models match those of the experimental studies, yielding stress values that are very close to the experimental results. The calibrated CM was utilized to study three additional finite element analysis (FEA) models: (a) Half-Diameter Stirrups in the Beam (HDB), (b) Half-Diameter Stirrups in both Beam and Columns (HDBC), and (c) Double Spacing of Stirrups in Beam and Columns (DSBC). This assessment focused on measuring the influence of critical design parameters, such as transverse reinforcement ratio (ρt), on the load-carrying capacity of DSSB, especially in a brittle manner. The findings confirmed that all the new FEA models exhibited less lateral load than CM, -4.45%, -13.8% and -5.2% respectively of HDB, HDBC, and DSBC.

It should be noted that experimental validation is available only for the CM (Control Model) configuration. The parametric variants (HDB, HDBC, and DSBC) represent numerical investigations comparing ANN-FEA predictions against ABAQUS and SAP2000 results. Therefore, findings for these variants should be interpreted as comparative assessments among numerical models rather than experimentally validated conclusions. The percentage differences reported for these variants reflect the agreement between different numerical approaches rather than experimental accuracy.

## 3. Database of RC beams

### 3.1. Description and Statistical Characterization of the Databases

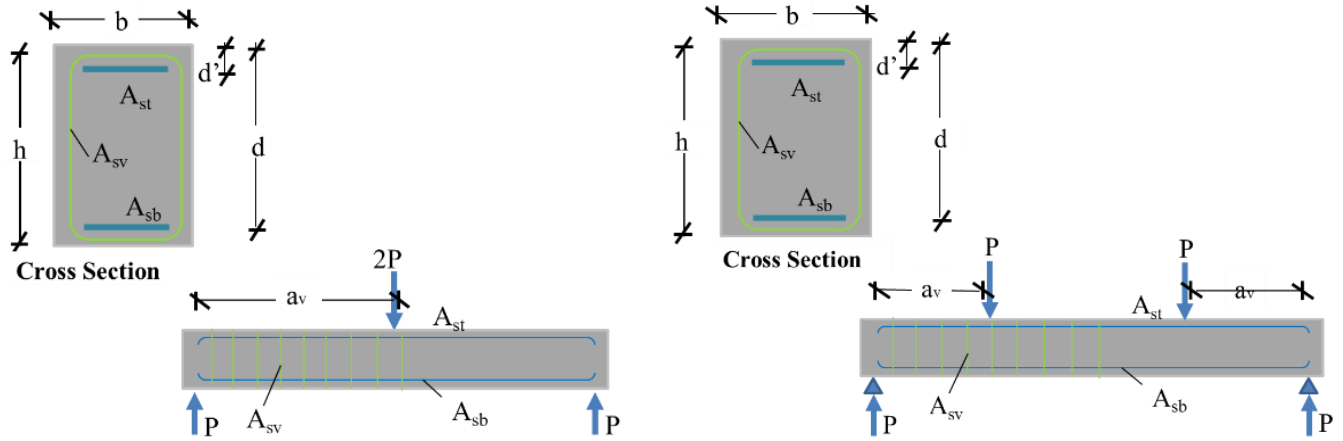


**Fig. 2**. Experimental setup for RC Beams (a&b)

**Table 1.** Statistical information for the for BWS

| | b | d | $a_v/d$ | $\rho_l$ | $f_{yl}$ | $f_c$ | $\rho_w$ | $f_{yw}$ | $M_f$ | $V_u$ |
|---|---|---|---|---|---|---|---|---|---|---|
| **Unit** | mm | mm | | (%) | MPa | MPa | (%) | MPa | kN-mm | kN |
| **Min** | 100 | 113 | 1 | 0.18 | 250 | 13.8 | 0.08 | 224 | 2648 | 4.097 |
| **Max** | 510 | 975 | 7.25 | 5.6 | 890 | 126 | 2.25 | 875 | 1,738,423 | 760.194 |
| **Avg.** | 208 | 343 | 3.5 | 2.4 | 415 | 45 | 0.6 | 400 | 283,485 | 185.54 |
| **St. Dev** | 68 | 158 | 1.5 | 1.1 | 78 | 25 | 0.5 | 115 | 378,729 | 134.25 |
| **COV** | 0.34 | 0.48 | 0.4 | 0.46 | 0.2 | 0.55 | 0.9 | 0.3 | 1.35 | 0.75 |

The initial phase of this study involves developing Artificial Neural Network (ANN) models for reinforced concrete (RC) beams and columns. Two databases have been established: (i) RC beams with Stirrups (BWS) and (ii) RC columns with Axial Load (CWA). The BWS database consists of 315 RC beam specimens subjected to 3-point or 4-point loading tests, as shown in Fig. 2 (a&b). It provides insights into how design parameters affect the load-carrying capacity and failure modes of RC beams approaching the Ultimate Limit State (ULS). Key features include

material properties, geometric dimensions, reinforcement details, loading conditions, and failure modes. Table 1 offers statistical information about specific parameters for the specimens, with 65% (204 samples) exhibiting shear failure modes and 35% (111 samples) demonstrating flexural failure modes. Fig. 3 presents a histogram illustrating the frequency distribution of key parameters in the BWS database. Additionally, this histogram indicates a limitation of ANN models, which are constrained by the parameter limits.

The second database comprises 130 samples of reinforced concrete (RC) columns (CWA) with cantilever support conditions, as shown in Fig. 4. Table 2, provides statistical data regarding the parameters associated with the CWA samples. Among these, 62% (80 samples) exhibit shear failure modes, while 38% (50 samples) display flexural failure modes. Fig. 5 presents a histogram illustrating the critical parameters for the CWA, showing the frequency distribution of each parameter across different sample values. This histogram also underscores a limitation of the ANN models, as the established limits of each parameter constrain their predictions.

### 3.2. Correlation Coefficient of the Parameters

The Pearson correlation coefficient (r) was calculated using Eq: 1 [66-69]. quantifies the linear relationship between pairs of variables within a dataset. For the BWS database, Fig. 6 (a) displays the correlation factors (r) for key parameters (b, d, $a_v/d$, ρl, $f_{yl}$, $f_c$). In contrast, Fig. 6 (b) presents those for the CWA database (b, d, $\rho_l$, N, $f_{yl}$, $f_c$, $\rho_w$, $f_{yw}$, $a_v/d$. These correlations guide the development of ANN models to predict the load-carrying capacities of RC specimens. The coefficient (r) ranges from -1 to 1, where negative values indicate an inverse relationship (an increase in one variable leads to a decrease in the other). In contrast, positive values indicate a direct relationship (where both variables increase or decrease together). A stronger linear dependence between variables is reflected by a higher absolute value of (r), meaning parameters with larger (r) exhibit a more significant influence on the load-bearing capacity predictions.

$$r=\frac{n\Sigma xy-(\Sigma x)(\Sigma y)}{\sqrt{n(\Sigma x^2)-(\Sigma x)^2}\sqrt{n(\Sigma y^2)-(\Sigma y)^2}} \quad \text{Eq: 1}$$

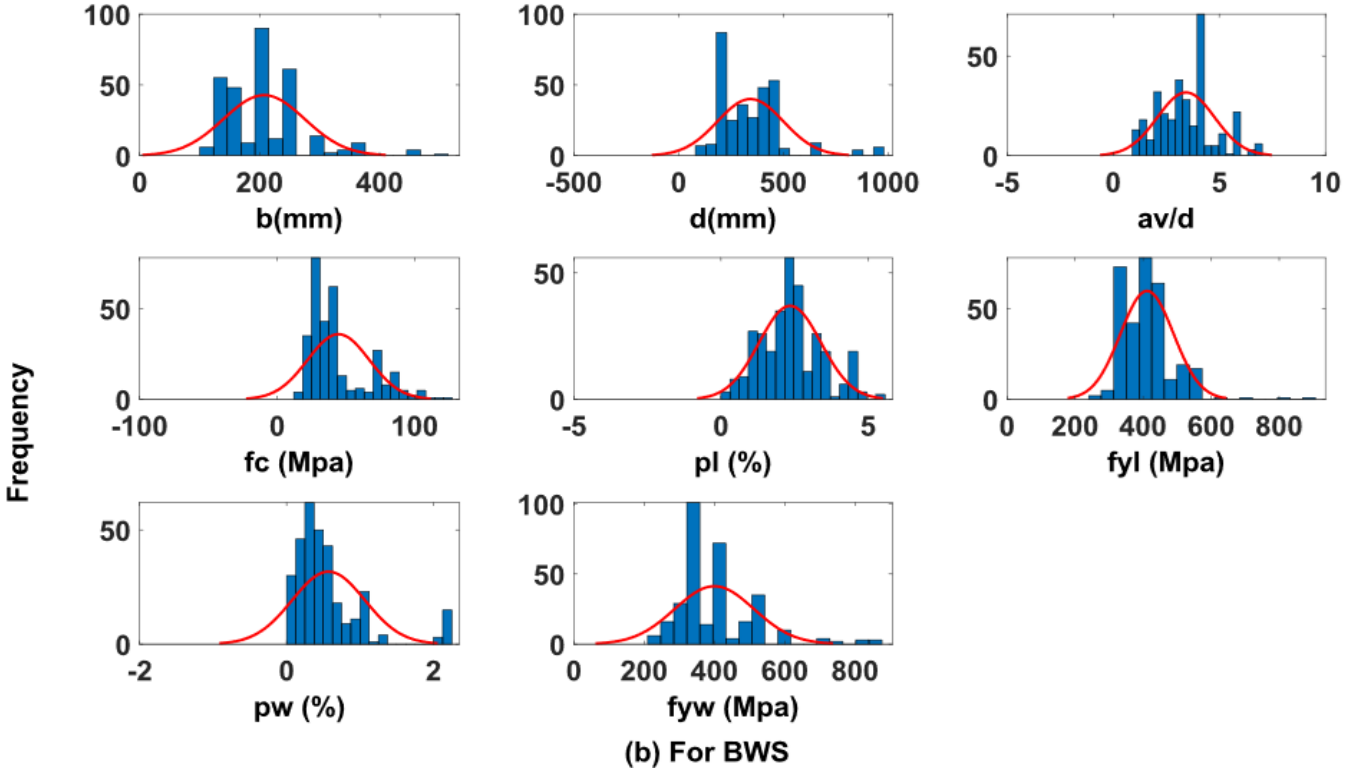


**Fig. 3**. Histogram of BWS Parameters

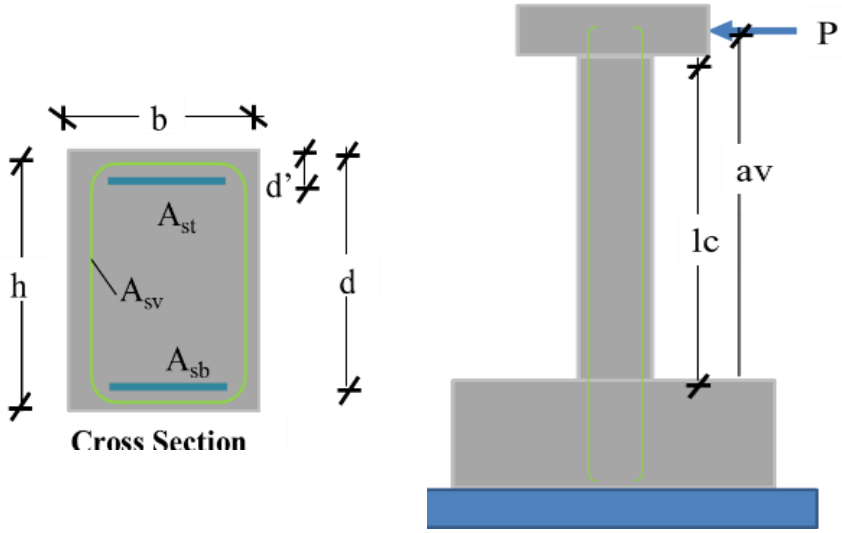


**Fig. 4.** Experimental setup for RC columns (CWA)

**Table 2.** Statistical information for the for CWA

| | b | d | $a_v/d$ | $\rho_l$ | $f_{yl}$ | $f_c$ | $\rho_w$ | $f_{yw}$ | N | $M_f$ | $V_u$ |
|---|---|---|---|---|---|---|---|---|---|---|---|
| | (mm) | (mm) | | (%) | (MPa) | (MPa) | (%) | (MPa) | (kN) | kN-mm | (kN) |
| **Min** | 150 | 110.5 | 2.647 | 0.87 | 313 | 17.9 | 0.1 | 255 | 111 | 15 | 33 |
| **Max** | 550 | 470 | 8.73362 | 6.16 | 559.5 | 118 | 2.8 | 1424 | 5373 | 1590 | 812 |
| **Avg.** | 323.03 | 241.22 | 5.1 | 3.19 | 463.16 | 49.09 | 0.82 | 497.46 | 1445.62 | 366.91 | 244.04 |
| **St. Dev** | 117.16 | 77.37 | 1.57 | 1.15 | 50.13 | 28.23 | 0.58 | 246.1 | 1270.2 | 337.62 | 177.62 |
| **COV** | 0.36 | 0.32 | 0.31 | 0.36 | 0.11 | 0.58 | 0.71 | 0.49 | 0.88 | 0.92 | 0.73 |

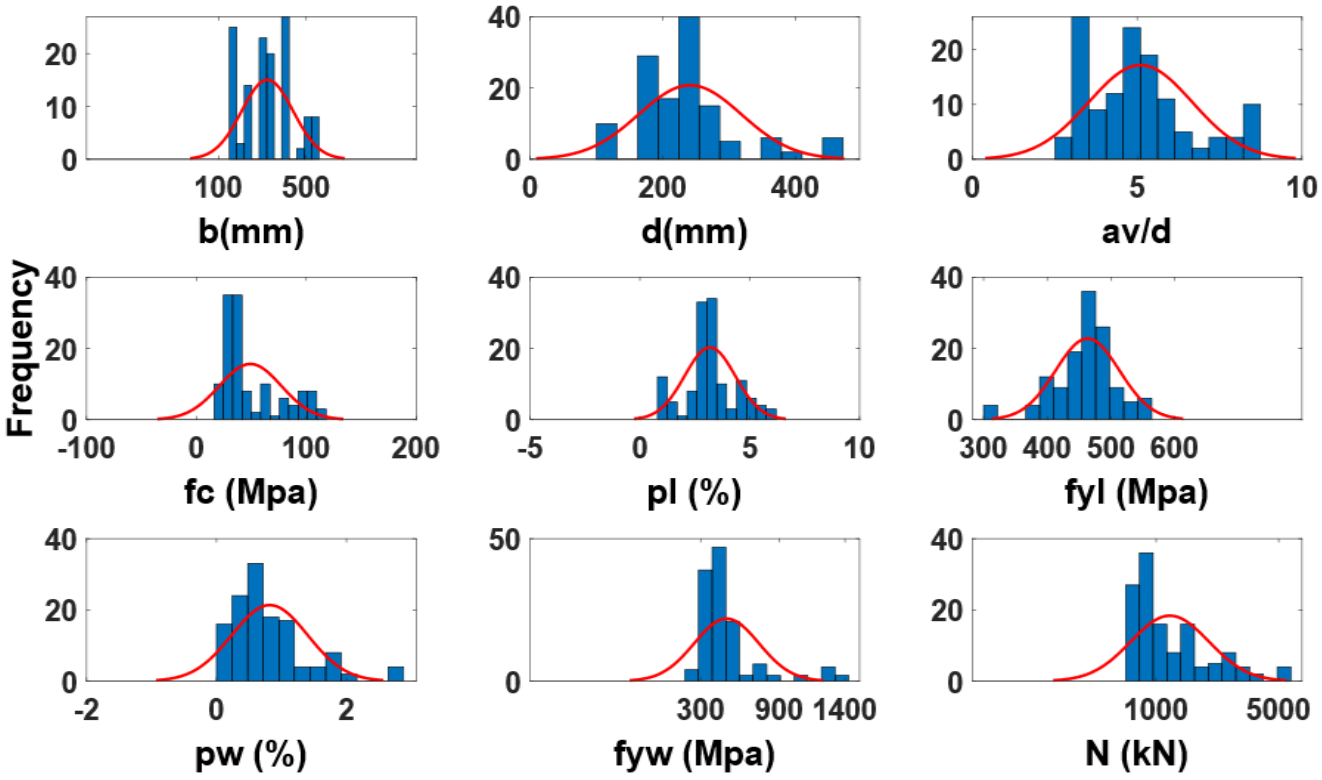


**Fig. 5.** Histogram of CWA Parameters

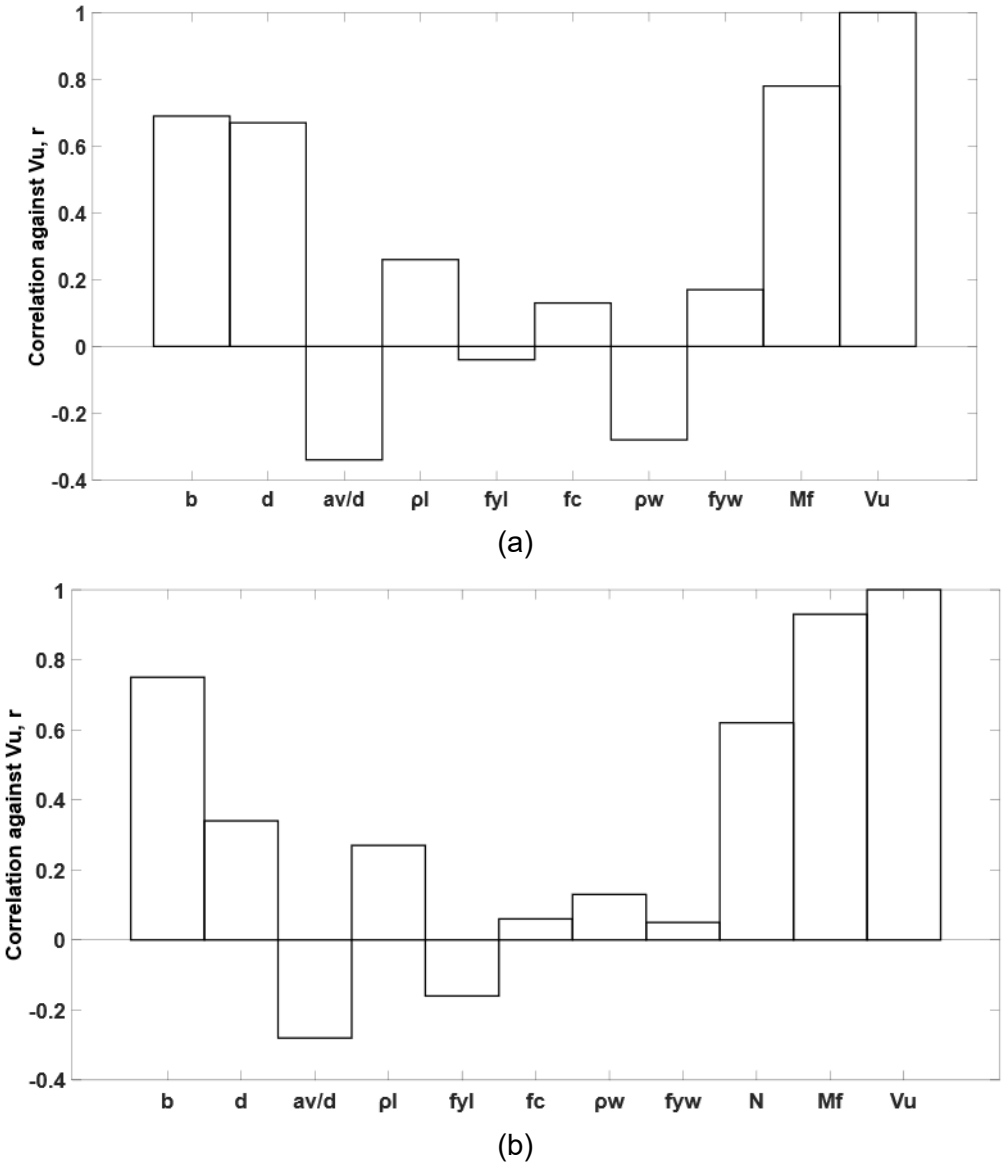


**Fig. 6.** The correlation parameter r (a) for BWS and (b) for CWA

## 4. Artificial neural network (ANN)

Research [55,59,70] indicates that Artificial Neural Networks (ANNs) are designed to emulate the structure and functionality of biological neural systems in living organisms (illustrated in Fig. 7 a&b). These computational models excel at processing complex relationships through pattern recognition, leveraging acquired knowledge from training to perform tasks such as classification, prediction, and generalization. Structurally, ANNs consist of multiple layers containing interconnected processing units ("neurons") that form sophisticated networks. As depicted in Fig. 7 these inter-neuronal connections are governed by specific weighting values. The fundamental mathematical representation of an ANN is provided in Eq: 2. The researchers have provided a comprehensive description of both the operational mechanisms and the supervised training methodology employed in these networks.

$$O = f(\sum x_i w_i + b) \quad \text{Eq: 2}$$

The output of a neural network (O) is influenced by the combination of weights (wi), inputs (xi), and a bias term (b). Activation functions play a crucial role in shaping the network's performance; typically, logistic and hyperbolic functions are applied between the input and hidden layers, while hyperbolic functions are used between the hidden and output layers. To refine the network's predictions, a back-propagation

algorithm based on the delta rule is employed, which systematically updates the weights to reduce the discrepancy between the predicted output and the actual target value (T) obtained from the dataset. As depicted in Fig. 7 (a&b), this learning process proceeds iteratively from the output layer back through the network, continuing as described by Eq: 3 until the mean squared error (MSE) falls below a predefined threshold, thereby improving the model's accuracy [55,59,70].

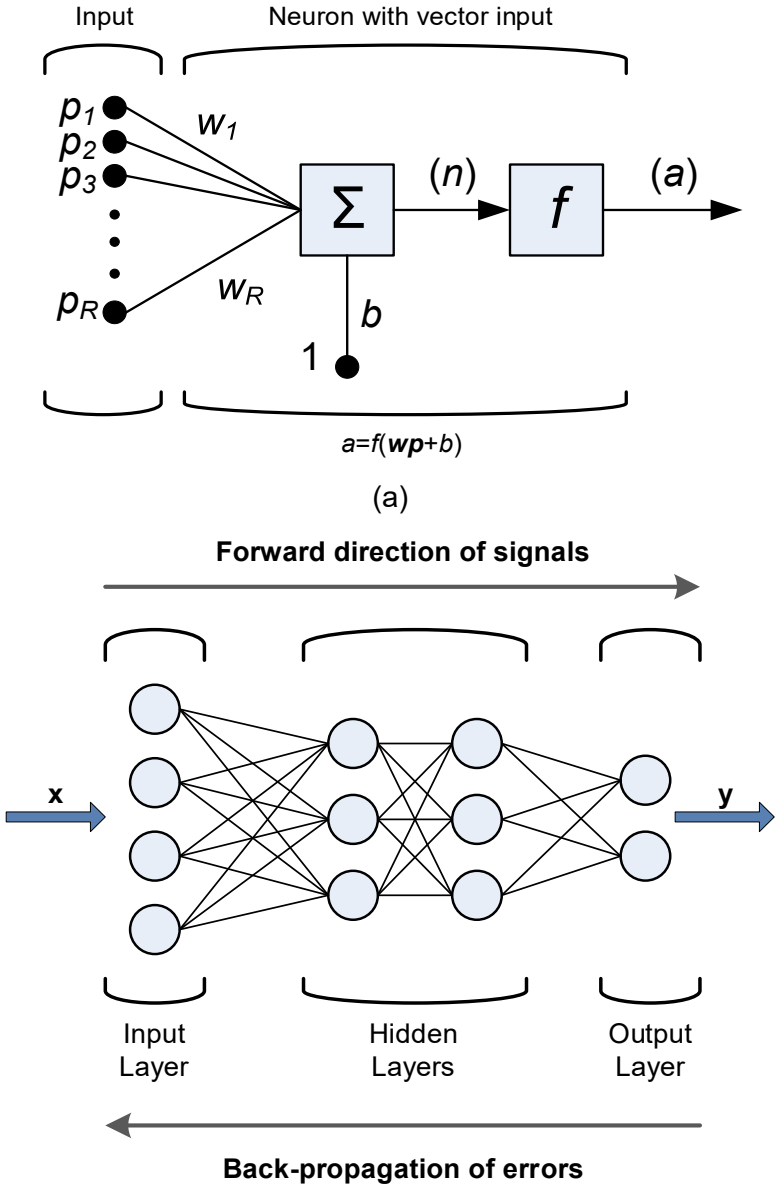


**Fig. 7.** (a) The Function of an Artificial Neuron and (b) Artificial Neural Network

$$E(w)=\frac{1}{2}\sum_i (T-O)^2 \qquad \text{Eq: 3}$$

The neural network's predicted output (O) is compared against the target values (T) from the database, and the resulting error is minimized through backpropagation using the Delta Rule [55,59,70]. This optimization process, illustrated in Fig. 7, involves iteratively adjusting initially randomized connection weights and propagating corrections backward (right to left) through the network to align the outputs more closely with the expected target values. Training continues until the mean squared error (MSE) converges to an acceptable threshold, indicating no further improvement. The fine-tuned weights are then applied in the ANN model, enabling more precise

predictions with reduced error margins.

### 4.1. Normalization of Database

Researchers [55,59,70] emphasizes that input normalization plays a critical role in training ANN models effectively, particularly when dealing with parameters of varying units. Normalization transforms all inputs into dimensionless values, improving computational efficiency and preventing sluggish learning rates. In this study, rather than using the standard 0 to 1 range, parameters are scaled between 0.2 and 0.8 Eq: 4 to enhance model performance [55,59,70]. The normalization process follows Eq: 4 where a raw input value (x) is converted to its normalized form (X) by referencing the maximum value ($x_{max}$) and the range ($x_{max}$ - $x_{min}$). This adjustment ensures smoother ANN training while maintaining numerical stability.

$$X=(0.6/\Delta)x+\{0.8-\left(\frac{0.6}{\Delta}\right)x_{max}\} \quad \text{Eq: 4}$$

### 4.2. Calibration of Proposed ANN Model

To ensure the accuracy of the proposed ANN model, calibration is performed by comparing its predictions with experimental results. The multi-layer feedforward backpropagation (MLFFBP) technique, introduced by Grossberg (1988) [71-75] is employed for this process, following established training methodologies [71-75]. To enhance generalization and prevent overfitting, the dataset is divided into three subsets: 60% for training, 20% for validation, and 20% for testing [71-75]. MATLAB [76] Serves as the computational platform for ANN implementation.

i. Each ANN model undergoes training for 100 epochs using the MLFFBP algorithm [71-75]. The iterative process terminates when any of the following criteria are met:

ii. The performance goal (deviation between output and target values) falls below 0.0001.

iii. The validation phase records 20 consecutive failures (no improvement in error reduction).

iv. The minimum performance gradient attains a threshold of $1.0 \times 10^{-10}$, as defined by the Levenberg-Marquardt backpropagation method [71-75].

This optimization leverages a second-order algorithm that incorporates second-derivative information for efficient weight adjustment. The ANN's predictive accuracy is evaluated using three key indicators:

a. Mean Squared Error (MSE, Eq: 5) – Quantifies the average squared deviation between predicted and target values.

b. Mean Absolute Error (MAE, Eq: 6) – Measures the absolute difference between predictions and experimental data.

c. Correlation factor (R, Eq: 7) – Assesses the linear relationship between target and predicted outputs, with higher values indicating stronger agreement.

These metrics, drawn from prior studies [71-75], ensure rigorous validation of the model's reliability across diverse scenarios.

$$MSE=\frac{\sum_{i=1}^{n}(T_i-O_i)^2}{n} \quad \text{Eq: 5}$$

$$MAE=\frac{\sum_{i=1}^{n}|T_i-O_i|}{n} \quad \text{Eq: 6}$$

$$R=\frac{\sum_{i=1}^{n}[(c-\bar{T})(O_i-\bar{O})]}{\sqrt{\sum_{i=1}^{n}(T_i-\bar{T})^2\cdot\sum_{i=1}^{n}(O_i-\bar{O})^2}} \quad \text{Eq: 7}$$

In the following equations, Oi denotes the predicted values generated by the ANN, while $T_i$ refers to the experimentally observed (target) values. The variable n represents the total number of samples. The symbol $\bar{T}$ indicates the mean of the experimental values, and $\bar{O}$ denotes the mean of the predicted values.

### 4.3. ANN model development

Eight artificial neural networks (ANNs) were trained to predict the load-carrying capacity of RC beams in the BWS category, utilizing various input parameter combinations outlined in Table 3. Similarly, nine ANN models were developed for the CWA category, as detailed in Table 4. The final

columns of both tables present the architecture of each ANN model, specifying the number of neurons in the input layer, the two hidden layers, and the output layer (I-H-H-O format).

**Table 3.** ANNs architecture for BWS

| ANN Models | Combination of Parameters | I-H1-H2-O |
|---|---|---|
| BWS-1 | b, d, $\rho_l$, $f_{yl}$, $f_c$, $\rho_w$, $f_{yw}$, $a_v/d$ | 8-16-16-1 |
| BWS-2 | b, d, $M_f$, $f_c$, $\rho_w$, $f_{yw}$, $a_v/d$ | 7-14-14-1 |
| BWS-3 | b/d, $M_f/f_{cbd^2,}$, ρw, $f_{yw}$, $a_v/d$ | 5-10-10-1 |
| BWS-4 | b/d, $\rho_w/\rho_l$, $f_c/f_{yw}$, $a_v/d$ | 4-8-8-1 |
| BWS-5 | d, $M_f/f_{cbd^2,}$, $f_c$, $\rho_w f_{yw}$, $a_v/d$ | 5-10-10-1 |
| BWS-6 | d, b/d, $M_f/f_{cbd^2}$, $\rho_w$, $f_{yw}$, $a_v/d$ | 6-12-12-1 |
| BWS-7 | d, b/d, $M_f/f_{cbd^2,}$, $f_c$, $\rho_w f_{yw}$, $a_v/d$ | 7-14-14-1 |
| BWS-8 | d, b/d, $M_f/f_{cbd^2,}$, $f_c$, $\rho_w f_{yw}$, $a_v/d$ | |

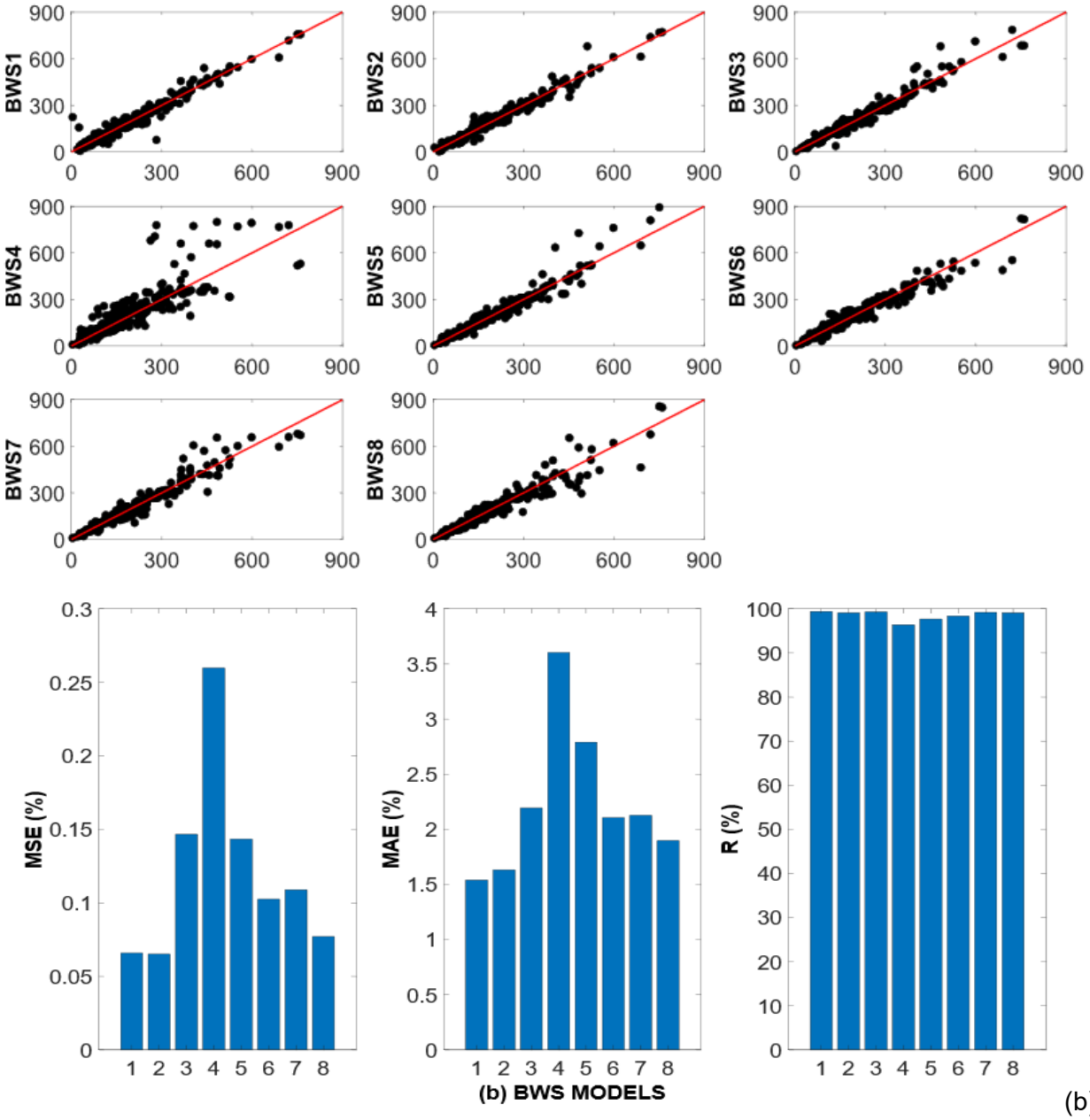


**Fig. 8**. (a) Results for BWS Models and (b) ANN performance for BWS

**Table 4.** ANNs architecture for CWA

| ANN Models | Combination of Parameters | I-H1-H2-O |
|---|---|---|
| CWA:1 | b, d, $\rho_l$, N, $f_{yl}$, $f_c$, $\rho_w$, $f_{yw}$, $a_v/d$, | 9-18-18-1 |
| CWA:2 | b, d, $M_f$, N, $f_c$, $\rho_w$, $f_{yw}$, $a_v/d$, | 8-16-16-1 |
| CWA:3 | b/d, $N/bdf_c$, $\rho_w$, $f_{yw}$, $M_f/f_cbd^2$, $a_v/d$, | 6-12-12-1 |
| CWA:4 | b/d, $N/bdf_c$, $f_c/f_{yw}$, ρw/ρl, $a_v/d$, | 5-10-10-1 |
| CWA:5 | d, $N/bdf_c$, $\rho_w f_{yw}$, $M_f/f_cbd^2$, $f_c$, $a_v/d$, | 6-12-12-1 |
| CWA:6 | d, b/d, $N/bdf_c$, $\rho_w$, $f_{yw}$, $M_f/f_cbd^2$, $a_v/d$, | 7-14-14-1 |
| CWA:7 | d, b/d, $N/f_cbd$, $\rho_w$, $f_{yw}$, $M_f/f_cbd^2$, $f_c$, $a_v/d$, | 8-16-16-1 |
| CWA:8 | d, b/d, $N/f_cbd$, $\rho_w f_{yw}$, $M_f/f_cbd^2$, $f_c$, $a_v/d$ | 7-14-14-1 |
| CWA:9 | d, b/d, $\rho_w$, $f_{yw}$, $M_f/f_cbd^2$, $f_c$, $a_v/d$, | 7-14-14-1 |

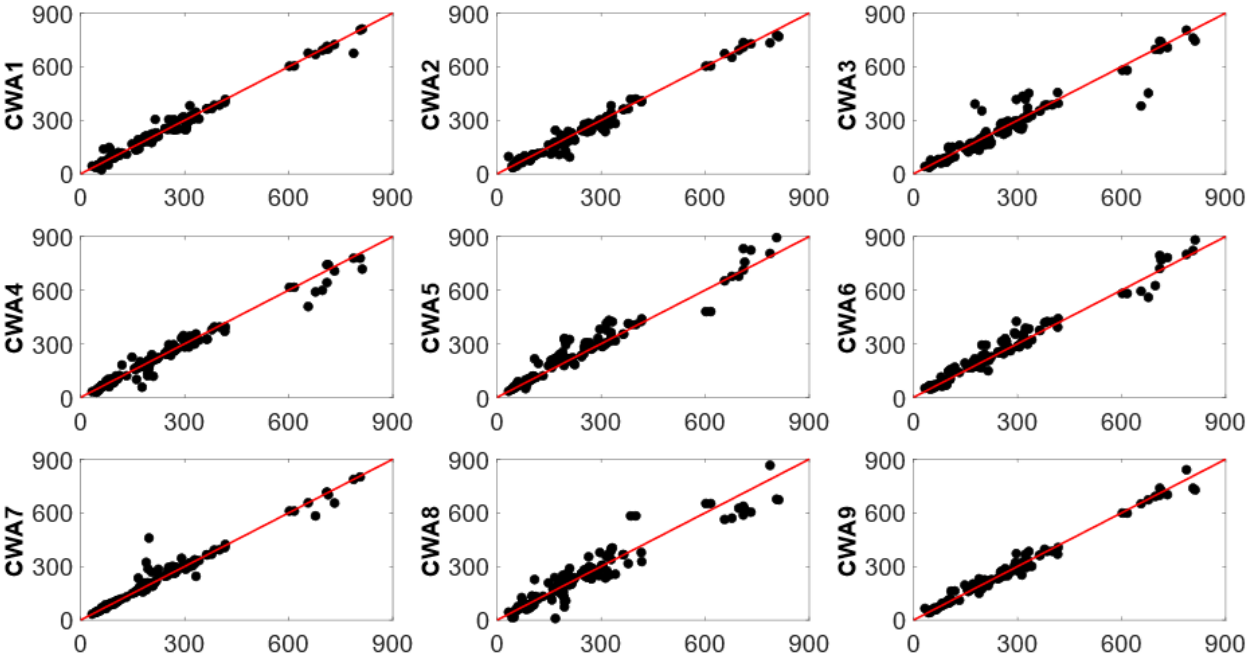


(a)

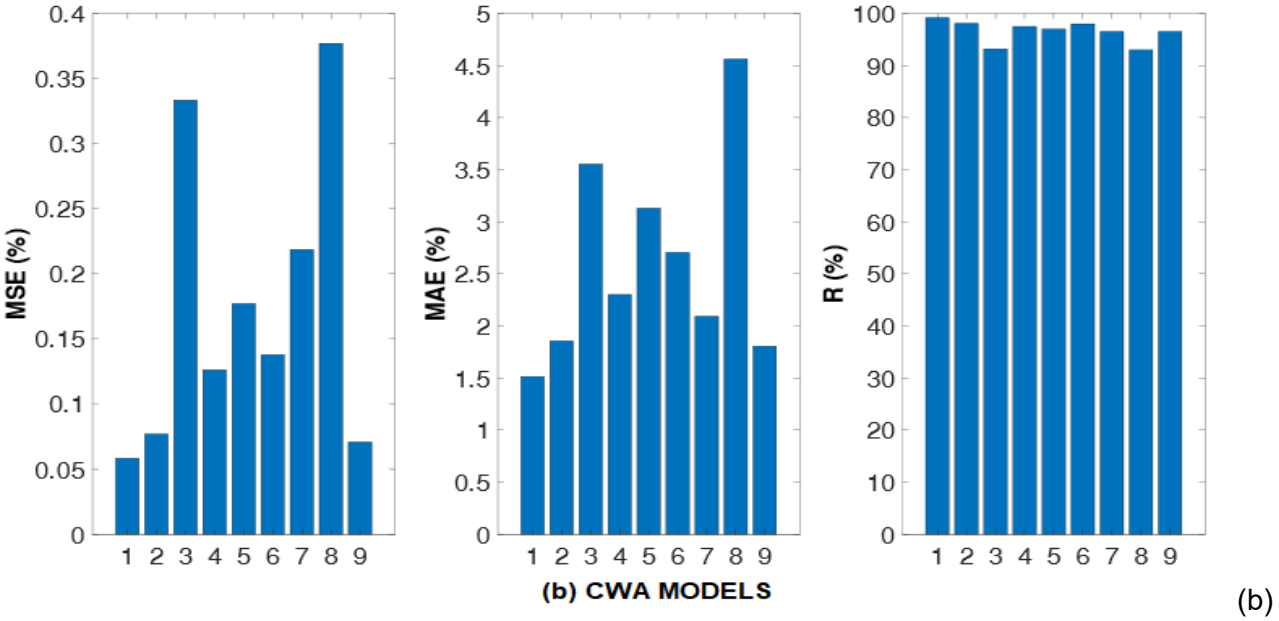


(b)

**Fig. 9**. (a) Results for CWA Models and (b) ANN performance for CWA

The selection of hidden layer neurons follows established guidelines in the literature, where the number of neurons in each hidden layer is typically set to approximately twice the number of input parameters to ensure adequate learning capacity while avoiding overfitting. This heuristic, combined with systematic testing of multiple architectures (as shown in Tables 3 and 4), allows identification of optimal configurations that balance model complexity with prediction accuracy. The final architecture selection was based on minimizing MSE and maximizing correlation coefficient R during cross-validation.

Fig. 8 (a&b) depict the performance of eight ANN models for predicting BWS, comparing their outputs with experimental data, while Fig. 9 (a&b). present nine ANN models for CWA. These figures also include error metrics: Mean Squared Error (MSE), Mean Absolute Error (MAE), and correlation coefficient (R) from references [55,59,70]. The models BWS-7, which uses input variables such as d, b/d, $a_v/d$, $M_f/f_{cbd^2}$, $f_c$, $\rho_w$, and $f_{yw}$, and CWA-8, incorporating (d, b/d, $N/f_{cbd}$, $\rho_w$, $f_{yw}$, $M_f/f_{cbd^2}$, $f_c$, $a_v/d$), are identified as the most optimal configurations for their respective predictions.

**5. Case study for DSSB**

To enhance the strength and stiffness of multi-story structures, which are particularly susceptible to seismic and wind forces, structural members are often designed with progressively larger cross-sectional dimensions from top to bottom. While this method bolsters structural integrity, it can lead to economic inefficiencies [65]. Therefore, integrating specialized mechanisms or systems to enhance lateral stability is crucial. Braced frames counteract lateral forces through the bracing action of diagonal members. Fully braced frames offer superior rigidity; however, from an economic standpoint, partially braced frames are more favorable as they generate minimal forces while keeping displacements within acceptable thresholds.

In 1980, a 12-story reinforced concrete building underwent retrofitting after a minor earthquake revealed significant seismic vulnerabilities. The retrofit involved bracing the perimeter frames along the building's weaker axis with an external steel truss system designed to withstand overturning forces, while also allowing access to the interior and underground parking [65]. The floor slabs were reinforced to transfer shear forces to these new frames. This study examines the structural behavior of steel and concrete cross-bracing, focusing on its effects on lateral load capacity and energy dissipation, and provides a comparative analysis with infilled frames. The findings offer insights into improving the lateral load resistance and overall performance of concrete frames. The experimentally validated Design-Sensitive Structural Behavior (DSSB) RC frame, as detailed in the study, includes design specifications of a 3500 mm center-to-center span and a story height of 2000 mm, culminating in a total frame height of 4600 mm [65]. All structural members maintained a uniform cross-section of 300 mm in width and 400 mm in depth, with reinforcement details documented in accompanying figures. Material testing indicated a concrete compressive strength of 30 MPa, whereas yield strengths of the steel reinforcement were recorded at 596 MPa (No.10 bars) and 640 MPa (No.20 bars). The testing procedure began with a constant axial load of 700 kN applied to each column, followed by a monotonically increasing lateral load under stroke-controlled conditions until the frame's ultimate capacity was reached. The global load-deformation behavior revealed significant relationships between applied lateral loads and top-frame displacements, with critical load stages identified [65].

The experimental setup and instrumentation for the tests are illustrated in Fig. 10. Initial cracking occurred at an applied load of 52.5 kN, with flexural cracks first emerging in the north section of the first-story beam. Further flexural cracking was noted at column bases under a load of 145 kN, coinciding with the development of initial web-shear cracks in the first-story beam. As the loading

continued, a progressive reduction in structural stiffness was observed due to extensive crack propagation. Strain gauge measurements indicated initial yielding at 264 kN in the bottom longitudinal reinforcement of the beam, followed by yielding of the top reinforcement at 287 kN.

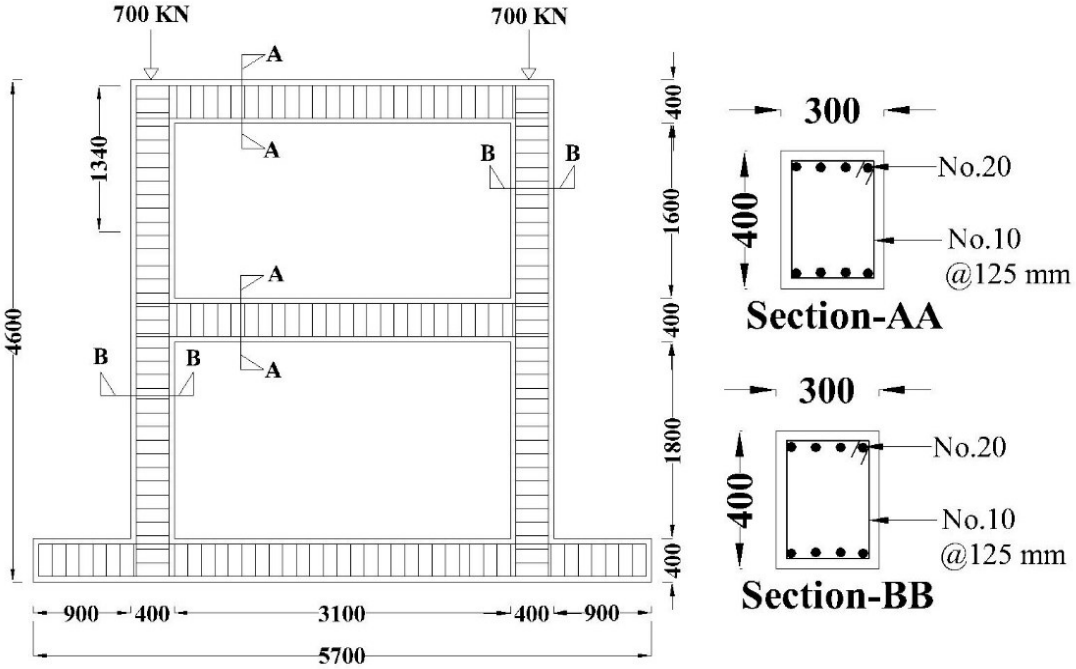


**Fig. 10**. Dimension and RCC details of the DSSB RC Frame

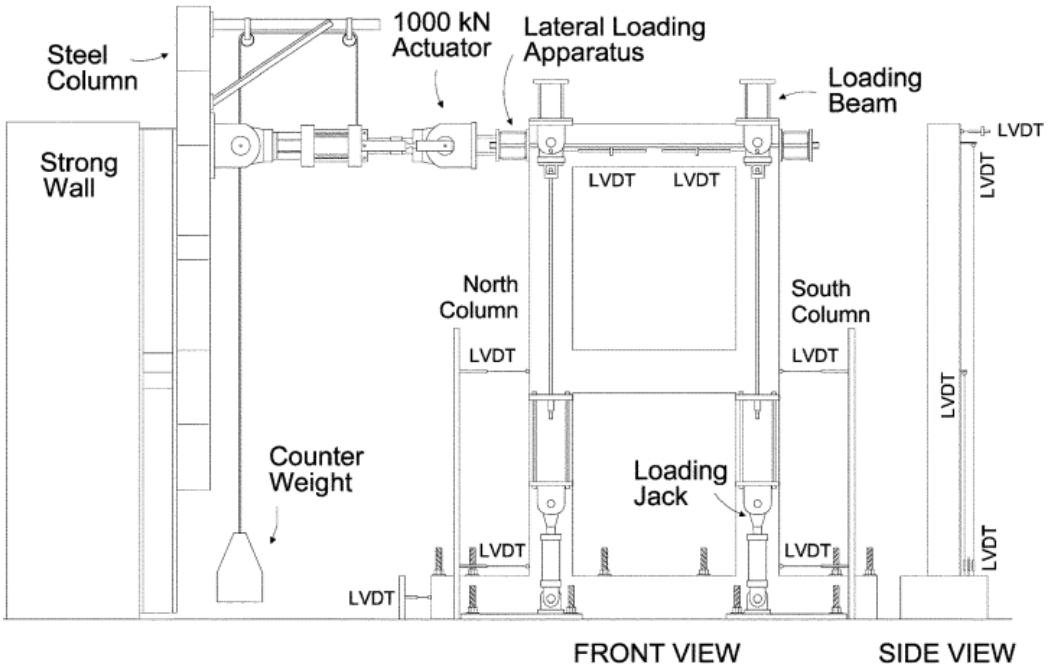


**Fig. 11**. Experimental results of DSSB RC Frame [65]

## 6. Finite element analysis of RC structural configurations

ABAQUS [8] recognized for its advanced finite element analysis (FEA) capabilities and accuracy in modelling materials such as concrete and steel [8,9] was employed to develop finite element models that capture the behavior of RC frames with high precision. In this modelling approach, concrete was simulated using 3D solid stress elements, while the reinforcing bars were represented by wire elements capable of full 3D deformation. Reliable simulation results were

ensured by applying suitable boundary conditions and load setups that enabled the gradual and uniform application of loads. The model underwent calibration and refinement to incorporate key parameters, including the concrete's shape factor, viscosity coefficient, dilation angle, mesh type, and element size. This refined model then supported an extensive parametric study, which explored the influence of these variables on the behavior of RC frame, thereby improving the accuracy and generalizability of the numerical analyses.

### 6.1. Compressive uniaxial stress-strain relationship for concrete

Fig. 12 presents the simplified upper-bound tensile stress-displacement relationship employed in this study. The Continuous Plastic-Damage (CPD) [8] model necessitates the definition of several critical parameters. Notably, the viscosity parameter is essential for achieving a smooth material response in Abaqus/Standard, while the dilation angle, denoted as ψ, indicates the inclination of the failure surface concerning the hydrostatic axis. This dilation angle plays a pivotal role in governing plastic flow and the overall material behavior under applied loads.

The different concrete material properties used in ABAQUS Standard, defining materials and step modules, are given in Table 5. The elasticity modulus (Ec) of concrete was calculated using the ACI code given by Eq: 8

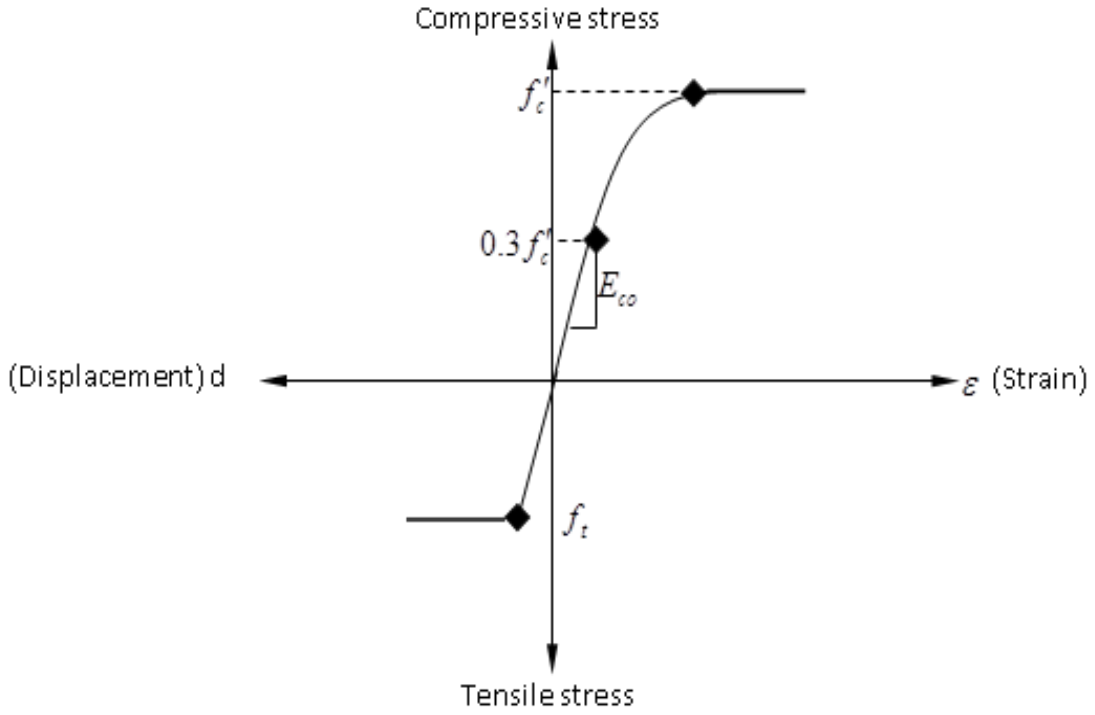


**Fig. 12.** Stress-strain curve of concrete used in the model [8]

**Table 5.** Different properties used in ABAQUS for concrete [8]

| Parameters | Values |
|---|---|
| Concrete density (ton/mm$^3$) | 2.4 X 10$^{-9}$ |
| Poisson's ratio, $\nu$ | 0.2 |
| Concrete Compressive Strength (MPa) | 35.06 |
| Elasticity modulus, $E_c$ (N/mm$^2$) | 26587 |
| The initial increment size of loading | 0.01 |
| Maximum increment size of loading | 0.1 |
| Minimum increment size of loading | 1E-050 |
| Number of increments | 100000 |

$$E_c=4700\sqrt{f_c'} \quad \text{Eq: 8}$$

The CPD model, originally developed for concrete, is also effective in simulating the behavior of other quasi-brittle materials such as masonry and mortar [8]. This model addresses two primary failure modes: tensile cracking and compressive crushing. Key inputs for the CDP model include the material's uniaxial stress-strain behavior in both tension and compression, as illustrated in Fig. 13 (a&b). In tension, the material exhibits a linear response until it reaches its peak tensile strength, after which it follows a softening curve. Conversely, in compression, it begins with a linear elastic phase, progresses into a hardening region, and eventually softens. These characteristics allow the CDP model to accurately represent the progressive damage and nonlinear response of quasi-brittle materials under various loading conditions.

The primary advantage of employing this material model is its ability to distinctly define the material's behaviour under tension and compression, thereby capturing its fundamentally different mechanical responses. This includes variations in yield strengths, tension softening, and the transition from hardening to softening in compression, as well as distinct elastic stiffness degradation under both tensile and compressive loads. The degradation of elastic stiffness in concrete is primarily attributed to failure mechanisms such as cracking under tensile stresses and crushing under compressive stresses. In the CPD model, this degradation is based on scalar-damage theory, where the loss of stiffness is considered isotropic and represented by a single scalar damage variable. The stress-strain relationship, incorporating this damage parameter as Eq: 9, is mathematically expressed in providing a concise representation of the material's behavior as it transitions from an undamaged to a damaged state.

$$\sigma=(1-d)\cdot D_0^{el}/(\varepsilon-\varepsilon^{pl})=D^{el}/(\varepsilon-\varepsilon^{pl}) \quad \text{Eq: 9}$$

In this context, $D_0^{el}$ represents the initial, undamaged elastic stiffness of the concrete, while $D_0^{el}=(1-d).D_0^{el}$ denotes the degraded elastic stiffness, accounting for material damage. The scalar variable ddd, which quantifies stiffness degradation, ranges from 0 ≤d≤1, indicates an entirely intact (undamaged) material and d=1 signifies a fully damaged state. The corresponding effective stress, which reflects the internal stress carried by the undamaged portion of the material, is formally defined in Eq: 10

$$\bar{\sigma}=D_0^{el}/(\varepsilon-\varepsilon^{pl}) \quad \text{Eq: 10}$$

and is related to the Cauchy stress through the scalar degradation variable as Eq: 11.

$$\sigma = (1-d)\cdot\bar{\sigma} \quad \text{Eq: 11}$$

The plasticity model of concrete is defined by various parameters, including the dilation angle (ψ), plastic potential eccentricity (ε), the ratio of biaxial to uniaxial compressive stresses ($\sigma_{b0}/\sigma_{c0}$), shape factor (Kc), and the viscosity parameter. The dilation angle and viscosity values were determined through calibration. According to the concrete damaged plasticity model, the recommended values for the shape factor (Kc) and eccentricity (ε) are 2/3 and 0.1, respectively. The stress ratio ($\sigma_{b0}/\sigma_{c0}$) is specified as 1.16, based on Eq: 12 proposed in reference [8], which quantifies this ratio using a substantial amount of statistical data.

$$\frac{\sigma_{bo}}{\sigma_{co}}=1.5(f_c')^{-0.075} \quad \text{Eq: 12}$$

Fig. 14 presents the compressive stress-strain relationship for concrete as outlined in Eurocode 2 [13]. According to the ABAQUS [8] the material exhibits linear elastic behavior up to approximately to $0.4f_{cm}$ [13] also provides empirical formulations, derived from experimental observations Eq: 13 and expressed in Eq: 14 to estimate the strain $\varepsilon_{c1}$ corresponding to the mean compressive strength of concrete and the ultimate strain $\varepsilon_{cu1}$.

$$\varepsilon_{c1}=0.0014(2-e^{-0.024f_{cm}}-e^{-0.140f_{cm}}) \quad \text{Eq: 13}$$

$$\varepsilon_{cu1}=0.004-0.0011(1-e^{-0.0215f_{cm}}) \quad \text{Eq: 14}$$

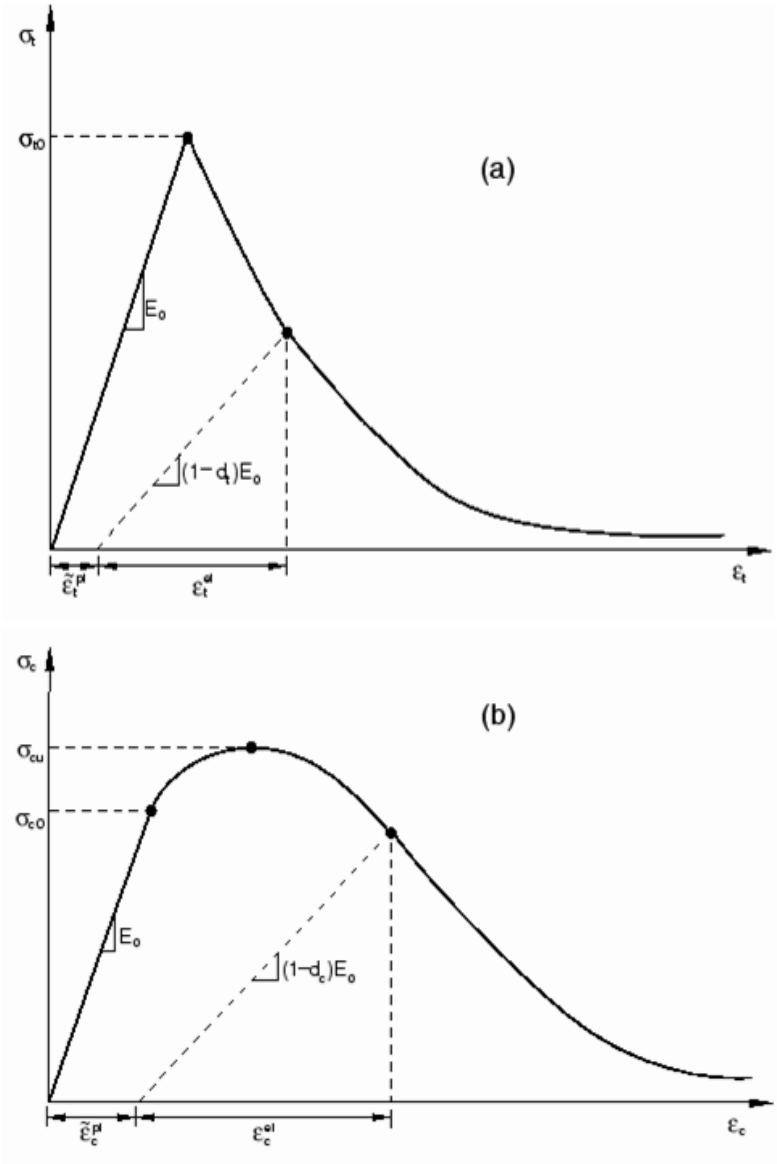


**Fig. 13**. CPD modelling (a) under tension and (b) under compression [8]

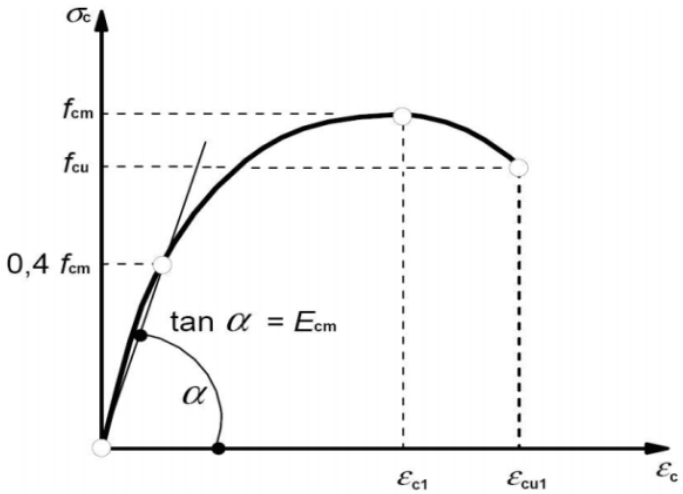


**Fig. 14**. Concrete modelling in ABAQUS [13]

### 6.2. FEM Modelling

The modeling process of the RC frame in ABAQUS involves defining the beam-column connections, where the column's bottom face is the

master surface and the beam's top face is the slave surface, as illustrated in Fig. 16 and Fig. 17. This same principle applies to the contact between the beam's top and the steel plates. The RC columns are fixed at the bottom, and a 60 mm thick rigid steel plate is attached to the top and sides of the beam using a 'tie constraint.' The steel plates are modeled as rigid elements with a Young's modulus of 210 GPa and a density of 7.85 × $10^{-9}$ ton/mm³. The finite element models for the steel-reinforced columns ensure that the top of the beam remains free in all directions during lateral loading, accurately representing support conditions.

The modeling of the steel cage within the DSSB RC frame is shown in Fig. 17 (a-d), Following ABAQUS guidelines, the steel mesh is embedded in the concrete (b), ensuring that the nodes of the reinforcing bar elements match the surrounding concrete's degrees of freedom (c). To evaluate the lateral load-deflection behavior of the DSSB RC frame until failure, a static load was applied on the left side of the beam using displacement control, with increments of 10 mm for gradual loading.

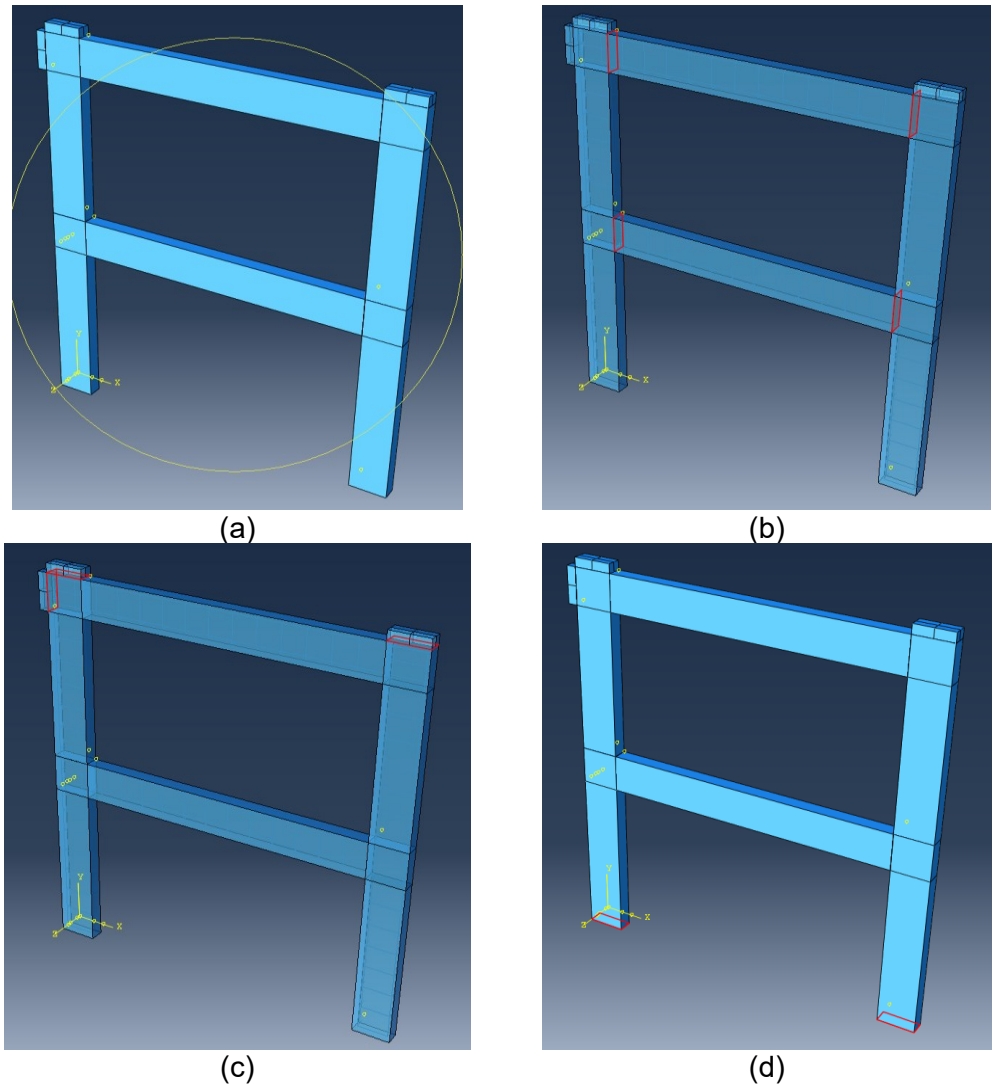


**Fig. 15**. Modelling of DSSB in ABAQUS (a) 3D model, (b) Connection between Beam & Columns, (c) Connection between steel plates and beam, and (d) Fixed support condition of Column

### 6.3. Calibration of CPD parameters

All the essential parameters required for defining the damage plasticity model, which describes the behavior of concrete, were calibrated using available experimental data. The calibrated values for these parameters are presented in Table 7. A static load was applied monotonically until failure, utilizing displacement increments under

displacement control. The graphs provided in Table 7 illustrate these parameters' numerical calibration. Only the target parameter was varied for each calibration, while all other parameters were kept constant.

The numerical load-deflection curves for the analysed RC beam were compared with the corresponding experimental results. Through the calibration process, the following parameter values were determined: (1) viscosity parameter, calibrated to 0.0028; (2) dilation angle, calibrated to 38°; (3) shape factor, calibrated to 0.677; and (4) stress ratio, calibrated to 1.0. These calibrated values reflect the material's response and are crucial for accurately simulating the behavior of RC frame under load.

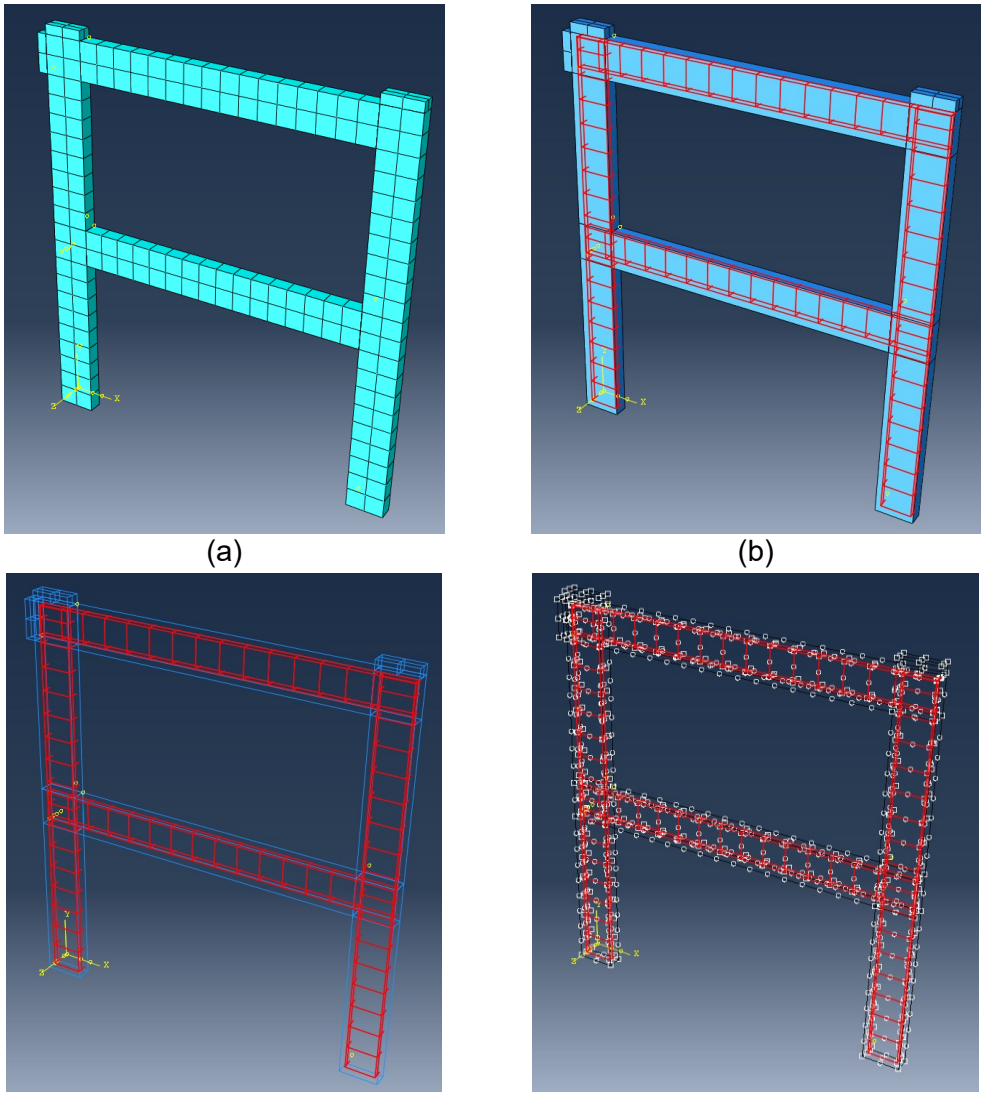

(a) (b) (c) (d)

**Fig. 16**. Modelling of DSSB in ABAQUS (a) Meshing of 3D model, (b) Steel Mesh in the frame, (c) Steel Mesh, and (d) Embedded steel mesh with concrete

**Table 7.** Concrete Damage Plasticity Parameters Used in ABAQUS Modelling [8]

| Sr. No | Descriptions | Values | Calibrated |
|---|---|---|---|
| 1 | Viscosity Parameter, **v** | 0.0018,0.0028,0.0038 | **0.0028** |
| 2 | Dilation Angle, **ψ** | 33°, 38°, 43° | **38°** |
| 3 | Shape Factor, $\mathbf{K_c}$ | 0.667, 0.9, 1.0 | **0.677** |
| 4 | Stress ratio, $\boldsymbol{\sigma_{b0}/\sigma_{co}}$ | 1.0, 1.16. 1.32 | **1.** |

The numerical load-deflection curves of the analysed RC frame, compared with their counterpart experimentally results, revealed the following calibrated parameter values: (1) a viscosity parameter of 0.0028, (2) a dilation angle of 38°, (3) a shape factor of 0.677, and (4) a stress ratio of 1.0. These calibrated values were derived based on the control model (CM) test results, as exhibited in Figs. 9 -12.

The calibrated CM was used for the numerical analysis of additional models, as outlined in the next section. Fig. 18 illustrates the impact of the viscosity parameter on the load-deflection response of the frame. The parameter's performance depends on the time increment size, with smaller values yielding better results alongside the pseudo-time scale of the finite element analysis. References [52,59,60,77-82] recommend a time increment step of about 15% of the pseudo-time for accuracy. In this study, the time increment was set to automatic with both initial and maximum sizes fixed at 0.01. The most accurate viscosity parameter value selected from 0.0018, 0.0028, and 0.0038 was 0.0028, calibrated with a constant dilation angle of 38° and a mesh size of 20 mm, ensuring consistent and reliable numerical modeling results.

The dilation angle represents the material's internal friction angle, influencing shear expansion during plastic deformation. Plastic Potential Eccentricity measures the convergence rate of the hyperbolic flow potential's asymptote, usually defaulting to 0.1 if not specified. The stress ratio denotes the compressive yield stress proportion in a biaxial state compared to a uniaxial state, typically set at 1.16. The shape factor (K), ranging from 0.5 to 1 (default 0.667), controls the yield surface shape in the deviatoric plane by defining the hydrostatic effective stress ratio between tensile and compressive meridians. Viscosity acts as a regularization factor in Abaqus/Standard analyses, stabilizing the solution by smoothing the constitutive response. The Drucker–Prager plastic potential function is mathematically defined by Eq. 15 and Eq. 16, where αp represents the dilatancy parameter for concrete. The flow potential function utilized in the CPD model is derived from the Drucker–Prager hyperbolic function [8].

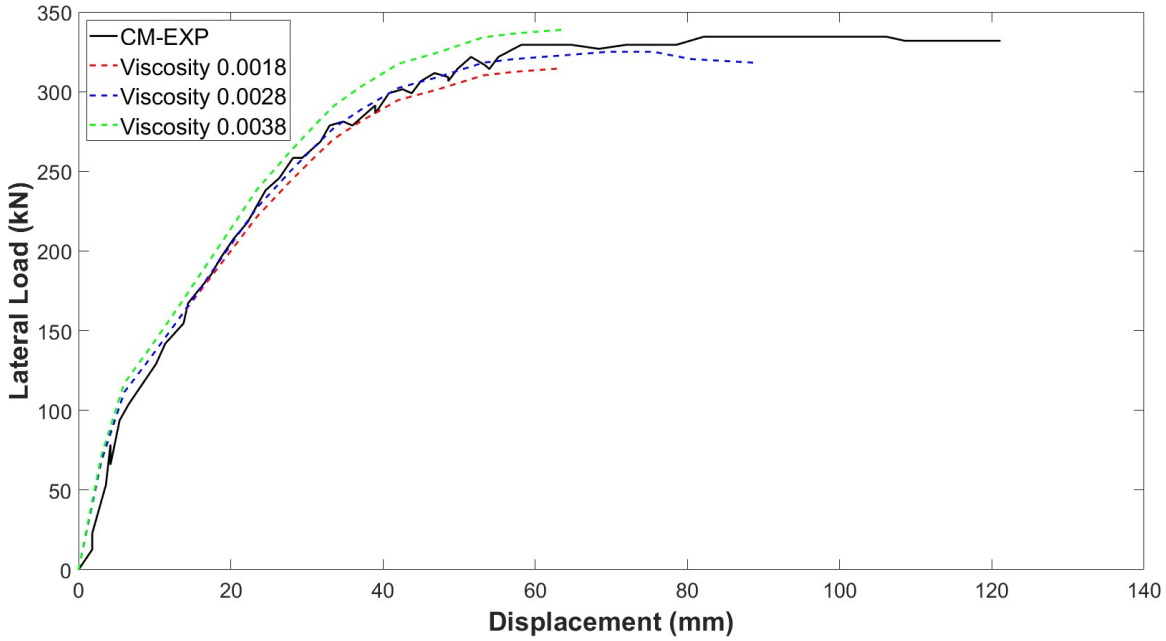


**Fig. 17**. Lateral load-axial deformation response of CM against different values of viscosity

$$G = \sqrt{2J_2} + \alpha_p I_1 \qquad \text{Eq: 15}$$

Using the Drucker–Prager plastic potential function, as defined by Lee and Fenves [8] in Eq: 16 the value of the dilation angle ψ is set to 38

$$G(\sigma) = \sqrt{(\varepsilon\sigma_{t0}\tan\psi)^2 + \bar{q}^2} - \bar{p}\tan\psi \qquad \text{Eq: 16}$$

In Eq: 16, ψ is the dilation angle, ε is the eccentricity of the plastic flow potential function needed to modify the shape of the hyperbola and $\sigma_{t0}$ is uniaxial tensile strength of concrete at failure can be rewritten as Eq: 17

$$G(\sigma)=\sqrt{(\varepsilon\sigma_{t0}\tan\psi)^2+\bar{q}^2}+\frac{1}{3}I_1\tan\psi \qquad \text{Eq:17}$$

For the considered range of $\alpha_p$, the dilation angle (ψ) is expected to lie between 31° and 42°. This study analysed dilation angles of 33°, 38°, and 43°. Parametric analysis demonstrated optimal correlation with experimental results when employing a dilation angle of 38° in conjunction with a viscosity parameter of 0.0028 and a mesh size of 20 mm. This calibrated configuration was consequently adopted for all subsequent finite element simulations. As shown in Fig. 19, the selected dilation angle significantly influences the axial load-deformation response, particularly for the CM where it accurately captures both the pre-peak stiffness and post-peak softening behavior observed experimentally. The load-deflection curves indicate that, although changes in the dilation angle affect the results, their influence is relatively minor compared to the significant effect of the viscosity parameter.

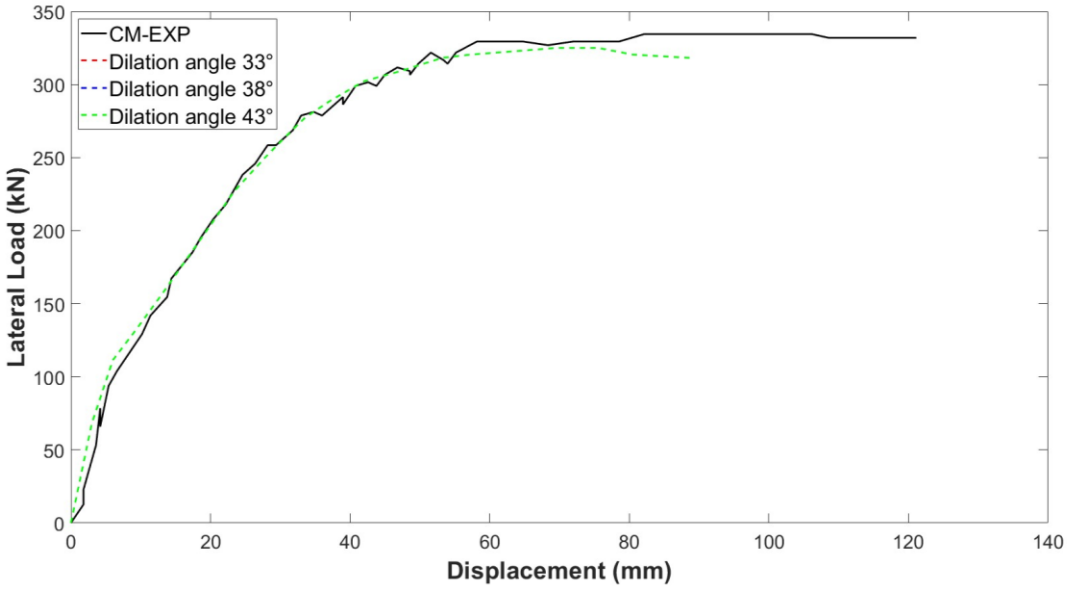


**Fig. 18**. Lateral load-axial deformation response of CM against different values of dilation angle

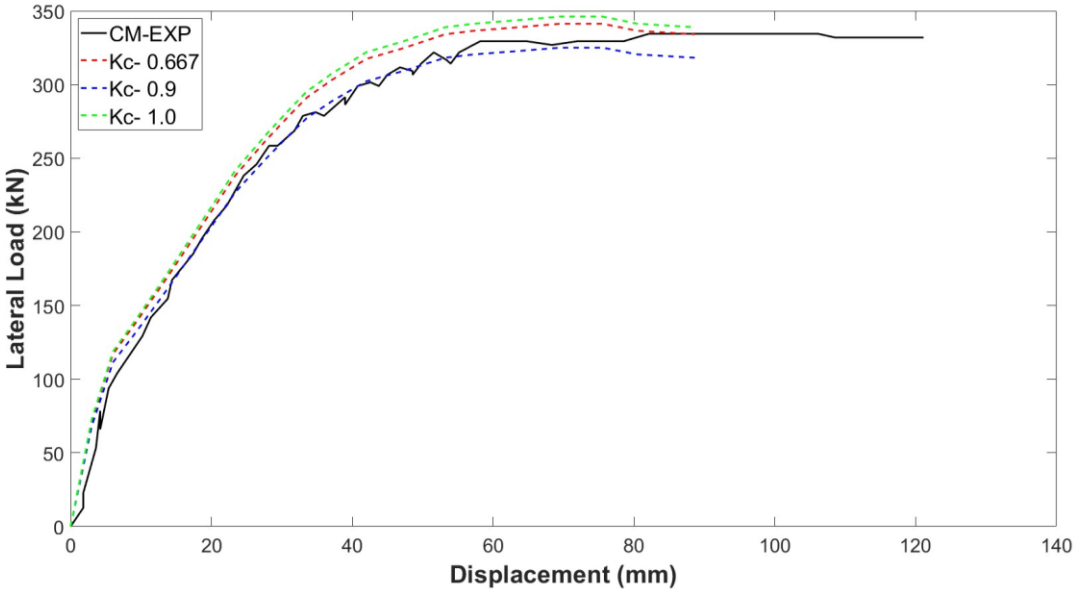


**Fig. 19**. Lateral load-axial deformation response of CM against different values of shape factor

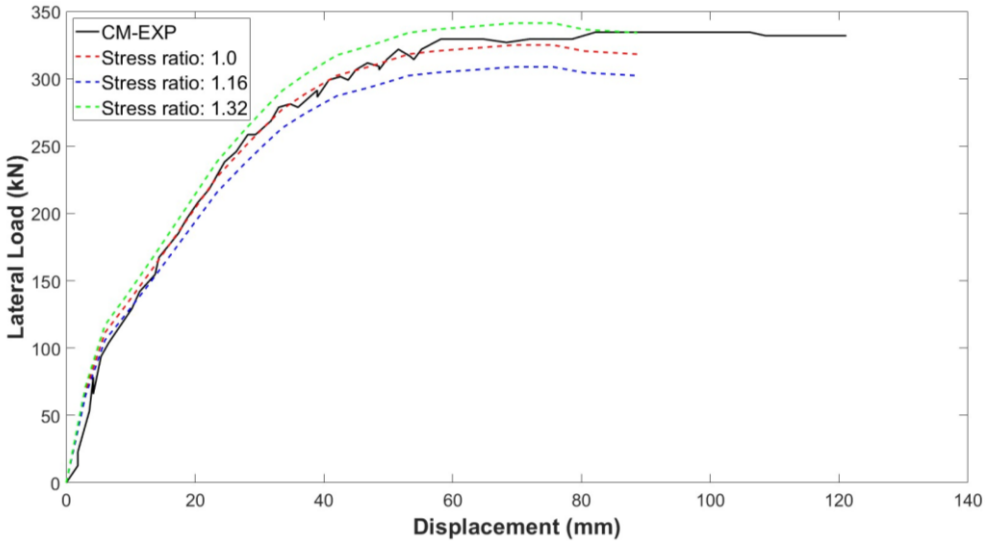


**Fig. 20.** Lateral load-axial deformation response of CM against different values of stress ratio

Fig. 20 shows the effect of different shape factor values (Kc) on the load-deflection behavior of the control specimen. The analysis includes three Kc values—0.667, 0.9, and 1.0—selected to explore the influence of the shape factor on structural response under load. The results reveal that increasing Kc does not significantly affect the load-displacement curve, as seen in Fig. 20. Therefore, Kc = 0.667 was chosen to optimize results while minimizing computational time for the CM.

For the calibration of the Stress ratio, $\sigma_{b0}/\sigma_{c0}$ [8] as shown in Fig. 21, the different values 1.0, 1.16, and 1.32 are used. However, all the values exhibited the same results. Thus, the value of 1.0 is used to get the optimized results and analysis time for the CM.

### 6.4. Stresses of Calibrated Model

Fig. 22 presents a finite element analysis from ABAQUS [8] of the DSSB RC Frame at the ultimate limit state (ULS), detailing its structural failure mechanisms. The figure illustrates the span-wise distribution of key parameters: vertical stress (S33) and strain (E33), which reveal tensile/compressive zones and deformation patterns; compressive damage (DAMAGEC), which highlights concrete degradation, especially at connections; and plastic equivalent strain (PEMAG), which signifies permanent inelastic deformation. A comparative plot of horizontal stress (S22), E33, and PEMAG further elucidates the interplay between stress, strain, and plastic response.

DSSB RC Frame is designated as the CM in this study, as it serves as a reference due to the availability of comprehensive experimental test data. During the loading process, the onset of flexural cracking was observed near the base of the columns when the top of the specimen underwent a horizontal displacement of approximately 6 mm. These initial cracks highlight the critical stress points at the base under early loading stages. As the lateral load increased, additional cracks were formed, predominantly in the regions surrounding the beam-column connections. This progression of cracking indicates significant stress concentrations at these junctions, emphasizing their role as vulnerable zones in the structural system under lateral loads. Under higher load intensities, diagonal cracks began forming toward the upper portions of the columns, eventually propagating into the beam-column joint areas. These observations highlight the progressive damage mechanisms and the vulnerability of the beam-column connections to shear and flexural stresses under lateral loading.

Fig. 23 ABAQUS [8] FEA results for reinforcement behavior in the DSSB RC Frame at ULS: (a) Axial Yield Criterion (AC Yield) showing initiation of steel yielding; (b) Maximum Principal

Stress (S, Max) highlighting critical tensile zones; and (c) a detailed plot of AC Yield and S, Max along the rebar, illustrating the progression of plastic deformation. Peak stresses and strains are localized at the column base and beam-column joints, with positive (+) and negative (-) values indicating tension and compression, respectively.

Fig. 24 and Fig. 25 present a comparative analysis between experimental findings and numerical predictions generated using SAP2000, ABAQUS, and the proposed ANN-FEA approach for the RC frame. Fig. 24(a) illustrates the experimentally observed crack propagation within the RC frame, while Fig. 24(b) The results from a pushover analysis conducted in SAP2000 highlight the location and type of plastic hinges at the ULS. Fig. 24(c) depicts the damage severity and distribution predicted by ABAQUS, and Fig. 24(d) displays the crack pattern forecasted by the ANN-FEA model, which closely aligns with the experimentally documented failure modes, demonstrating the reliability and accuracy of the proposed method. The results showed that ANN-FEA exhibits similar failure to ABAQUS, consistent with the experimental results. However, 2000 fails to predict the experimental results.

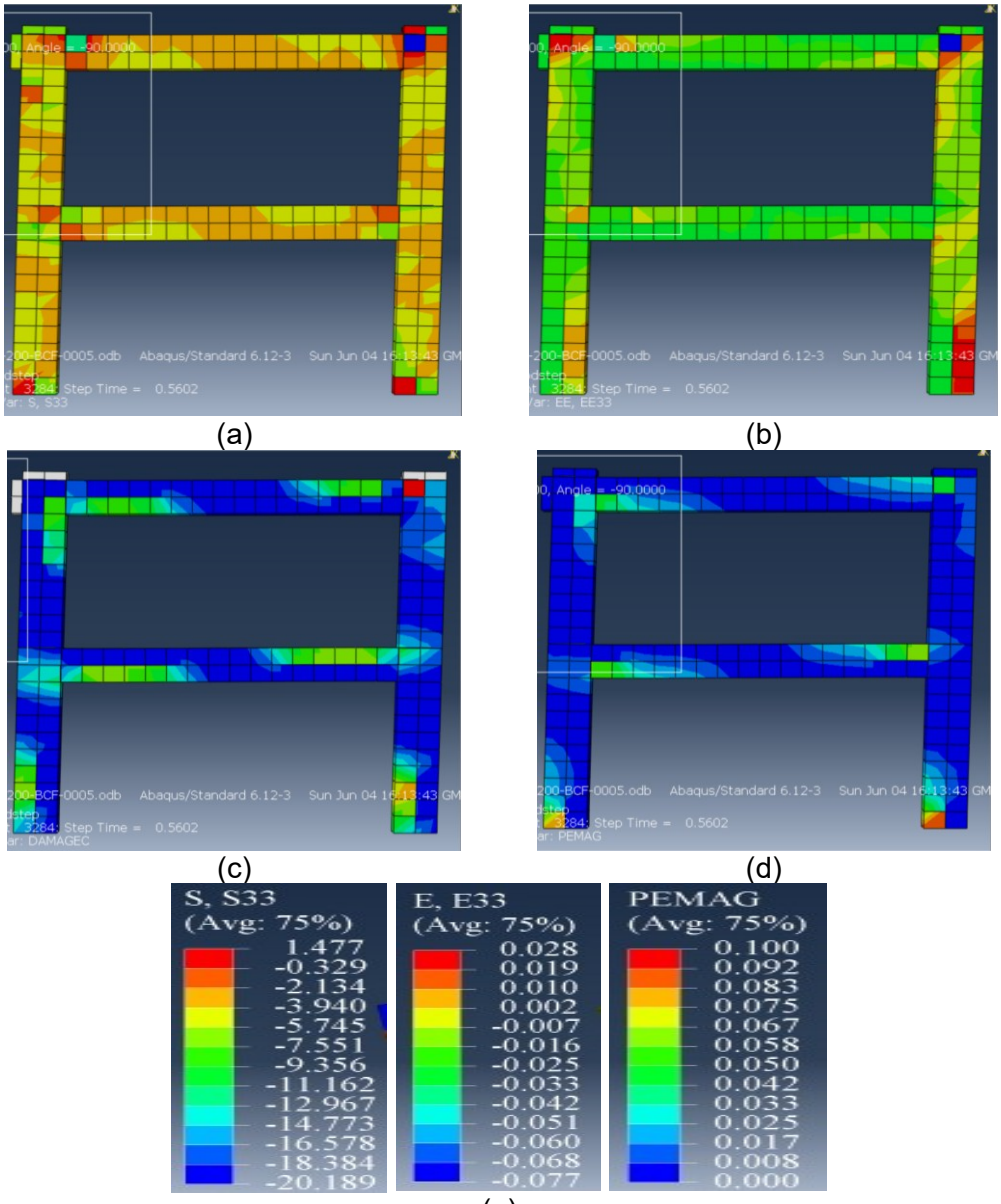


**Fig. 21**. DSSB RC Frame (a) Stress S33, (b) Strain E33, (c) DAMAGEC, and (d) PEMAG at ULS (e) Values for S22, E33, and PEMAG

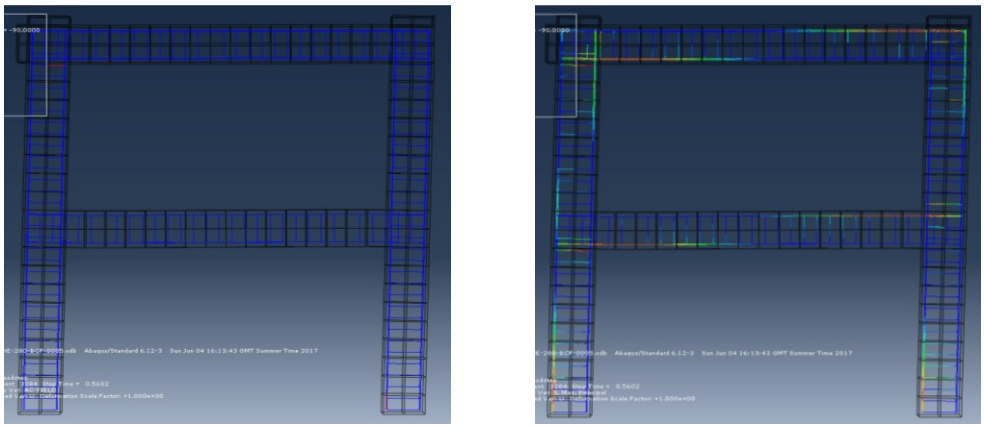

(a) (b)

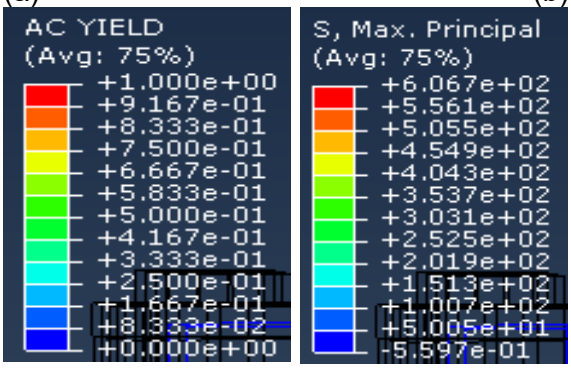


(c)

**Fig. 22**. DSSB RC Frame (a) AC Yield and (b) Max Principal Stress at ULS (c) Values for AC YIELD and S, Max

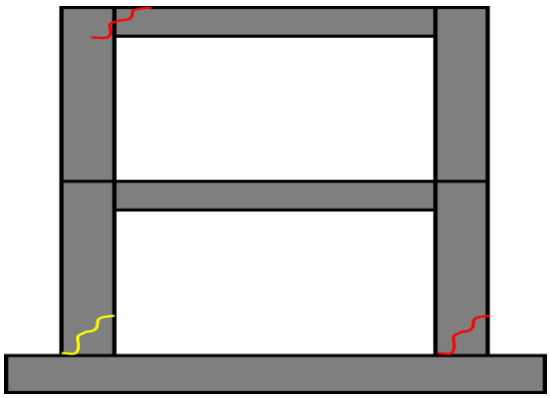

(a) Experimental Result

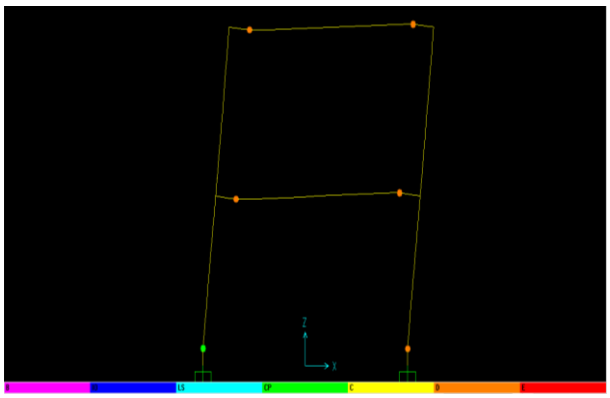

(b) SAP Result

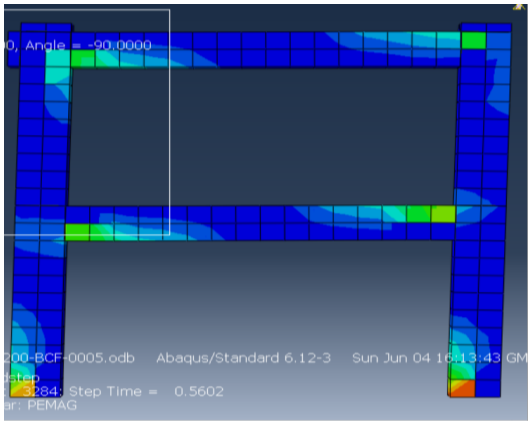


(c) ABAQUS Result

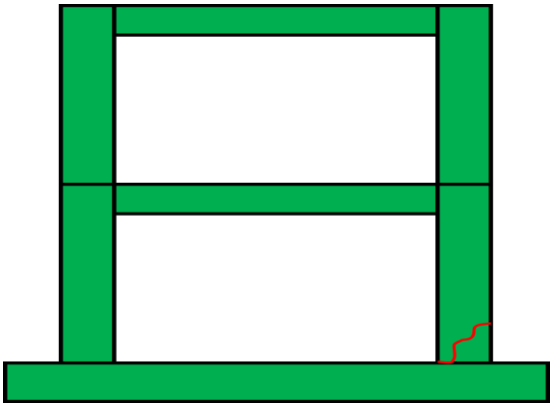

(d) ANN-FE Result

**Fig. 23**. Results of (a) experimental (b) SAP 2000, (c) ABAQUS for DSSB RC Frame, (d) ANN-FE

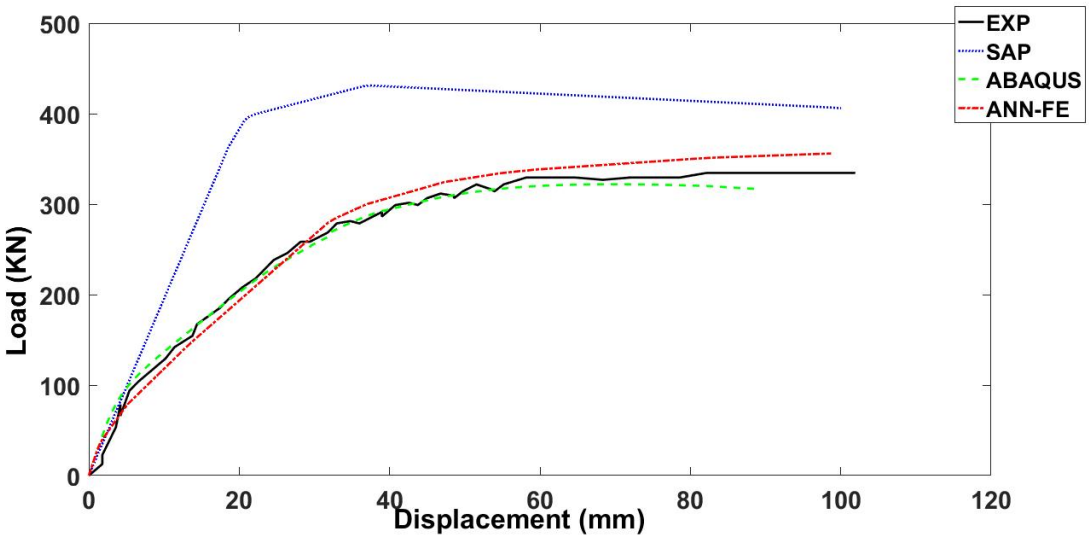


**Fig. 24**. Comparison of Load-Deflection curves for DSSB RC Frame at ULS

Fig. 25 presents a comparative assessment of load-displacement behavior obtained from experimental testing and various numerical approaches. The experimental curve, serving as the reference, demonstrates an initial linear increase in load with displacement, followed by a peak and a subsequent reduction, indicative of material softening or failure. In contrast, the results from the SAP2000 and ANN-FE methods exhibit higher load capacities at larger displacements, suggesting a stiffer response and delayed softening behavior. The ABAQUS model exhibits closer agreement with the experimental trend up to moderate displacement levels, but diverges beyond that point. Overall, the comparison highlights the variation in predictive accuracy among the methods, emphasizing the importance of model calibration and validation when simulating structural response.

## 7. New FEM models

To assess the impact of reinforcement detailing, a parametric study will analyze three numerical models derived from the calibrated Control Model (CM). Each model alters the transverse reinforcement to promote a shear-critical failure mode:

i. HDB: Features half the stirrup diameter in the beam only.

ii. HDBC: Uses half the stirrup diameter in both beams and columns.

iii. DSBC: Doubles the stirrup spacing in both beams and columns.

**Table 8.** Case Studies of SB RC Frame SF

| Sr. No | Description | Models |
|---|---|---|
| a. | Control Model | C.M |
| b. | Half Diameter of Stirrups Bars in Beam | H.D |
| c. | Half Diameter of Stirrup Bars in Beam & Columns | H.D.B.C |
| d. | Double spacing of Stirrups Rings in Beam & Columns | D.S.B.C |

Table 8 summarizes these case studies for short and slender RC (DSSB RC) frames under shear failure (SF) conditions, facilitating an understanding of how stirrup configuration influences structural behavior.

### 7.1. Half Diameter of Stirrup in Beam HDB

The HDB model, a modification of the DSSB RC Frame C-SF, investigates the effect of significantly reduced beam confinement. As detailed in Table 8, the transverse reinforcement in the beams was reduced by 75% compared to the original experimental frame. Fig. 26 illustrates this modified stirrup arrangement.

Fig. 27 illustrates the structural response of

the HDB specimen with reduced transverse reinforcement at the ultimate limit state (ULS), showing contours of vertical stress (S33) and strain (E33), compressive damage (DAMAGEC), and plastic strain (PEMAG).

Fig. 28 presents the ABAQUS FEA results for the HDB model's reinforcement at the ULS, showing the Axial Yield (AC Yield) and Maximum Principal Stress (S, Max) distributions. The contours identify where the rebar approaches its yield capacity, directly illustrating the impact of reduced beam stirrups on structural integrity under extreme loads.

Fig. 29 and Fig. 30 present a comparative analysis between experimental findings and numerical predictions generated using SAP2000, ABAQUS, and the proposed ANN-FEA approach for the HDB-SF. Fig. 29 (a) shows the results from a pushover analysis conducted in SAP2000, highlighting the location and type of plastic hinges at the ULS. Fig. 29 (b) depicts the damage severity and distribution predicted by ABAQUS, and Fig. 29 (c) displays the crack pattern forecasted by the ANN-FEA model. The results showed that ANN-FEA exhibits similar failure to ABAQUS. However, SAP2000 exhibited different results.

Fig. 30 compares the load-displacement responses of HDB-SF predicted by three computational techniques: SAP2000, ABAQUS, and ANN-FE. All approaches exhibit an initial linear relationship, indicating elastic behavior, followed by a gradual deviation as the displacement increases. The SAP2000 method predicts the highest load capacity at larger displacements, suggesting a stiffer structural response throughout the range. The ABAQUS simulation closely follows SAP2000 in the early and mid-stages but diverges slightly near the end. Meanwhile, the ANN-FE approach shows a sharper rise in load at smaller displacements. Still, it plateaus earlier than the other two, reflecting a different interpretation of material or structural behavior under increasing deformation. The variations among the methods underscore differences in modelling assumptions and computational strategies used in simulating the mechanical response.

### 7.2. Half Diameter of Stirrup in Beam and Columns HDBC

The HDBC model, which reduces transverse reinforcement by 75% in both beams and columns relative to the Control Model (CM), was analyzed to assess its impact on structural performance. Fig. 31 details the updated stirrup configuration, with the comparison to the CM underscoring the critical role of transverse reinforcement in maintaining frame stability, as outlined in Table 7.

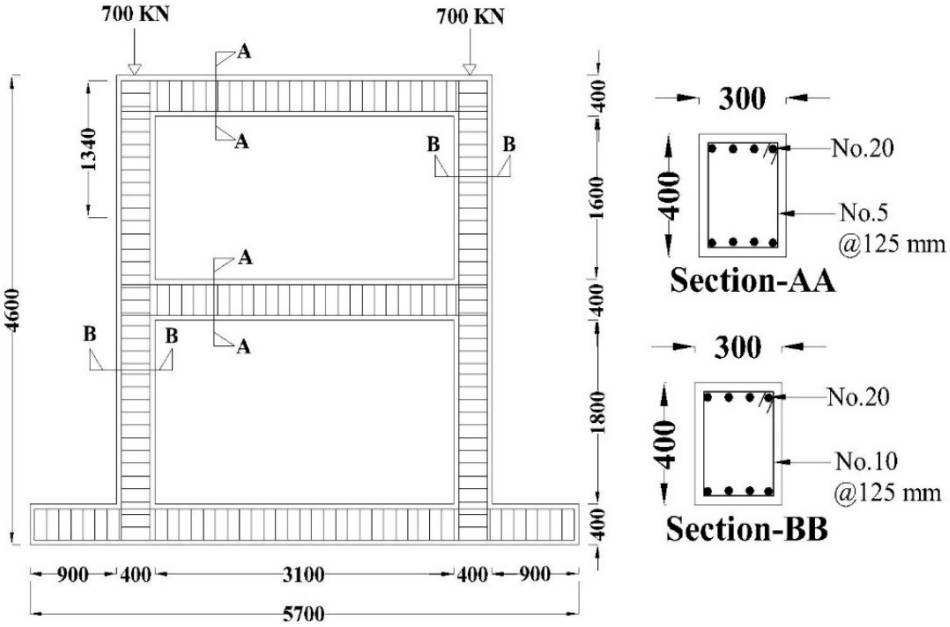


**Fig. 25**. Reinforcement details of HDB

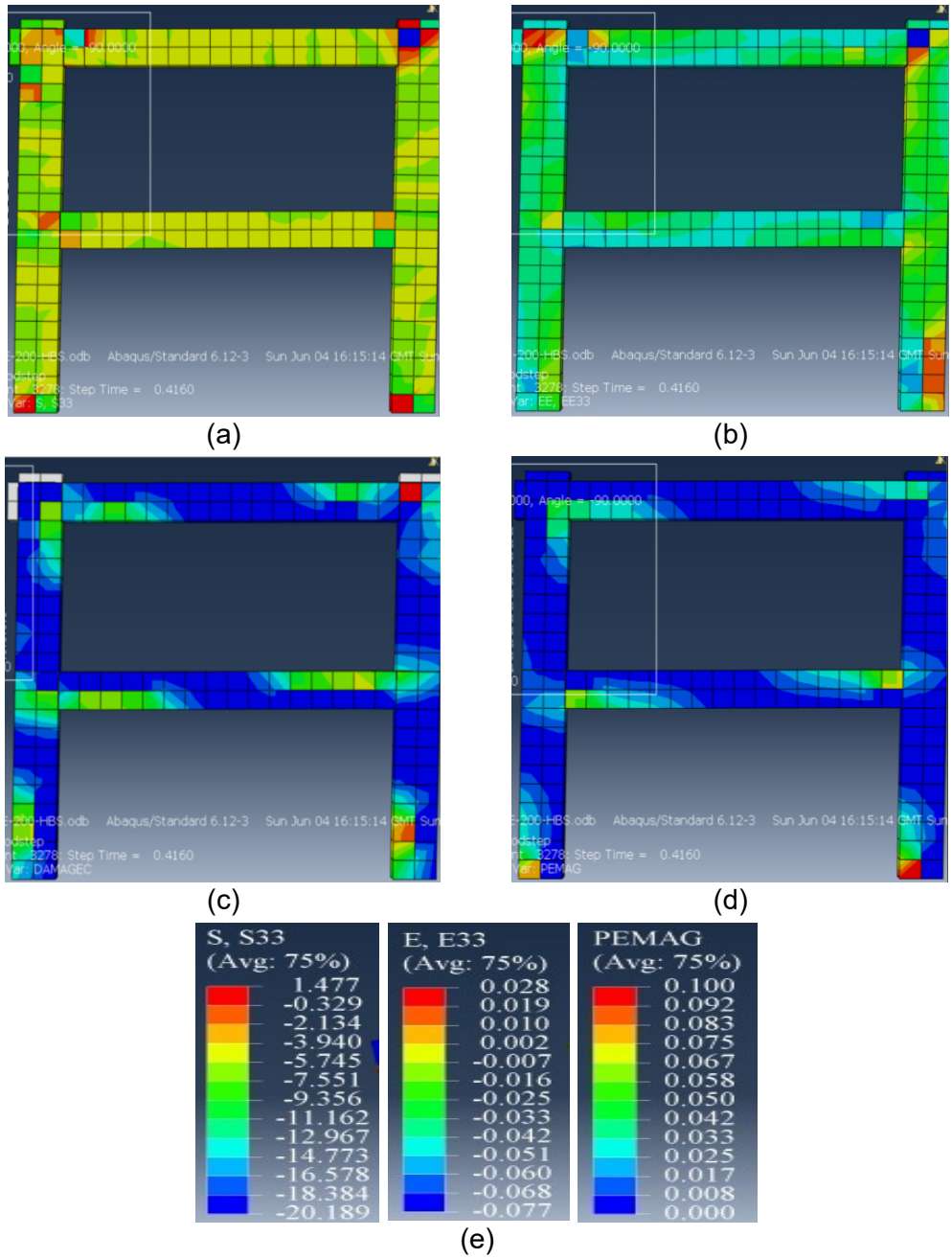


**Fig. 26**. HDB RC Frame (a) Stress S33, (b) Strain E33, (c) DAMAGEC and (d) PEMAG at ULS (e) Values for S22, E33 and PEMAG

Fig. 31 and Fig. 32 present the finite element analysis results for the HDBC model at the ULS. Fig. 31 shows the concrete response through contours of vertical stress (S33) and strain (E33), compressive damage (DAMAGEC), and plastic strain (PEMAG). Fig. 32 illustrates the reinforcement behavior, displaying the Axial Yield Criterion (AC Yield) and Maximum Principal Stress (S, Max).

Fig. 33 and Fig. 34 present a comparative analysis between experimental findings and numerical predictions generated using SAP2000, ABAQUS, and the proposed ANN-FEA approach for the HDBC. Fig. 33(a) shows the results from a pushover analysis conducted in SAP2000, highlighting the location and type of plastic hinges at the ULS. Fig. 33(b) depicts the damage severity and distribution predicted by ABAQUS, and Fig. 33 (c) displays the crack pattern forecasted by the ANN-FEA model. The results showed that ANN-FEA exhibits similar failure to ABAQUS. However, SAP2000 exhibited different results.

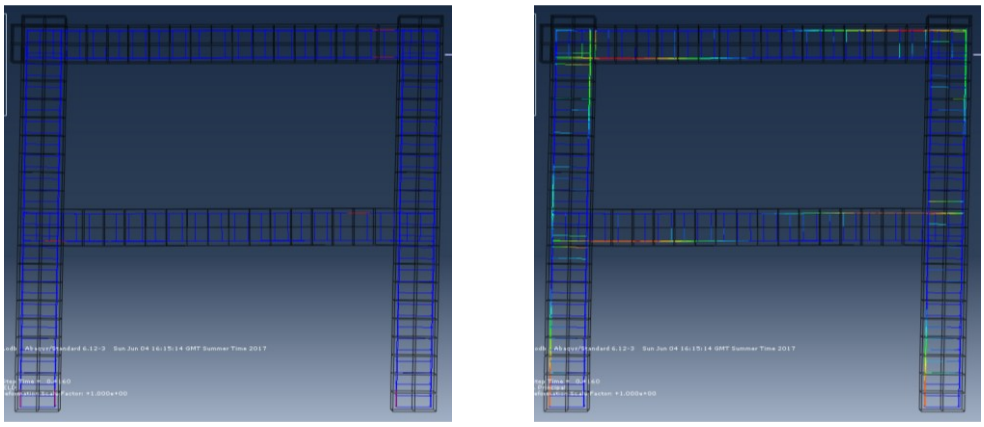

(a) (b)

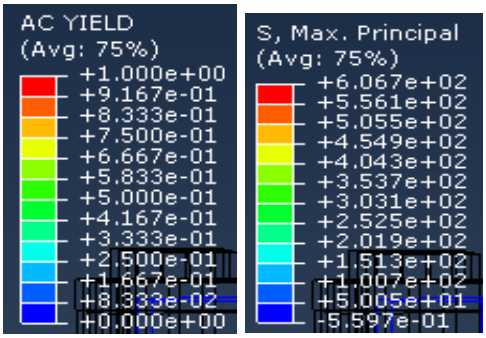


(c)

**Fig. 27**. HDB RC Frame (a) AC Yield and (b) Max Principal Stress at ULS (c) Values for AC YIELD and S, Max

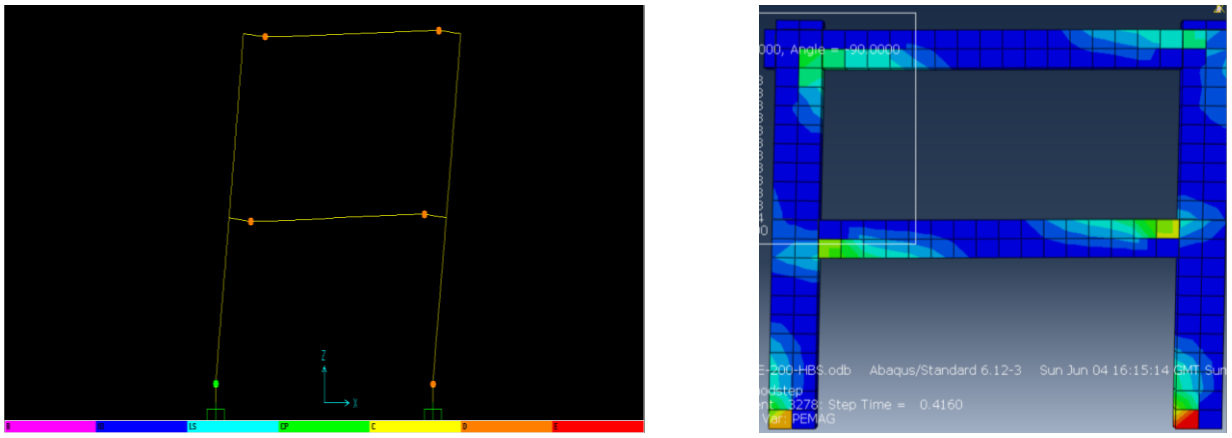

(a) SAP Result (b) ABAQUS Result

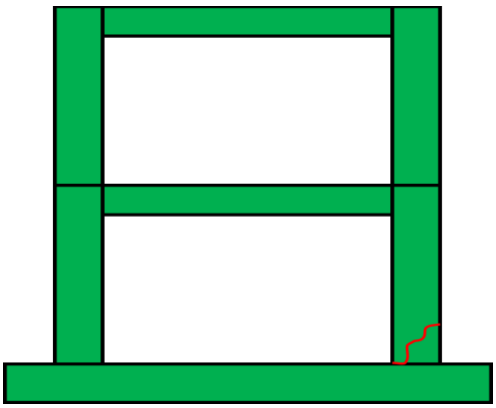

(c) ANN-FE Result

**Fig. 28**. Results of (a) SAP 2000, (b) for HDB at ULS, (c) ANN-FE

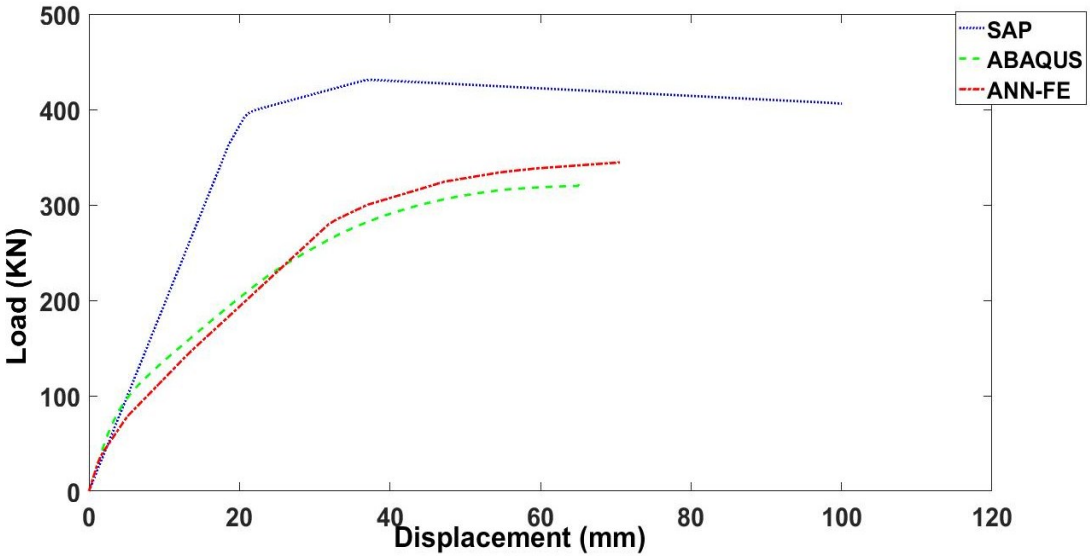


**Fig. 29**. Comparison of Load-Deflection curves obtained for HDB

Fig. 34 illustrates the load-displacement behavior as predicted by three numerical approaches: SAP2000, ABAQUS, and ANN-FE. All methods start with a linear rise in load, reflecting elastic performance. The SAP model demonstrates a continued increase in load capacity beyond 50 mm of displacement, indicating a more ductile or stiffer modelled behavior. ABAQUS and ANN-FE predictions, in contrast, extend only up to around 20 mm, showing an earlier levelling off or limit in their simulations. Among them, ANN-FE predicts higher initial stiffness and slightly greater peak loads than ABAQUS. The observed differences highlight the sensitivity of each modelling strategy to deformation and load progression, with implications for how each captures post-elastic response characteristics.

### 7.3. Double spacing of Stirrup in Beam and Columns DSBC

The DSBC model, which doubles the stirrup spacing in beams and columns, was analyzed against the Control Model (CM) to assess its structural impact. This change, detailed in Fig 35 and Table 8, effectively halves the transverse reinforcement volume, significantly influencing load capacity, ductility, and damage progression. The comparison underscores the critical role of stirrups in maintaining frame stability.

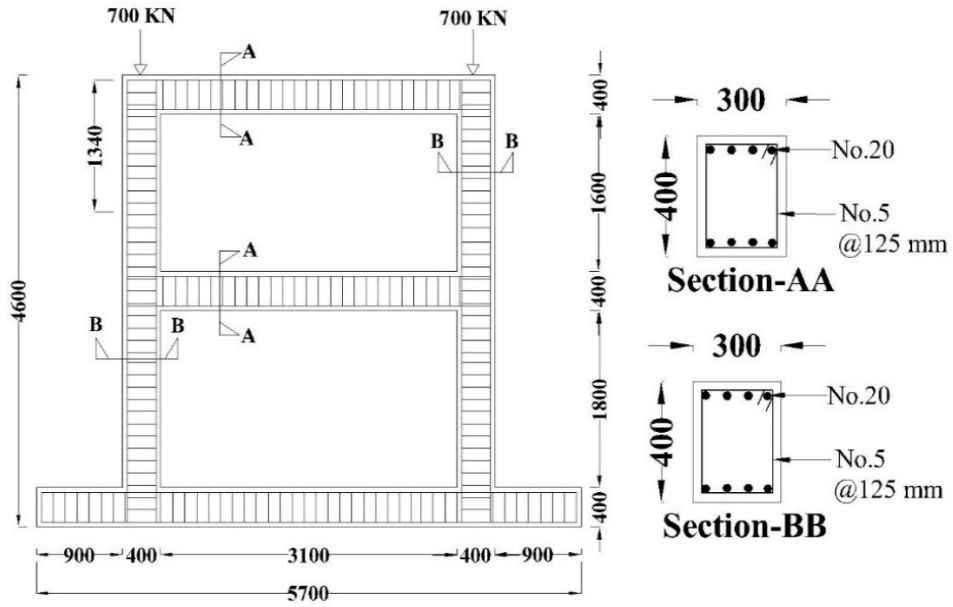


**Fig. 30**. Reinforcement details of HDBC

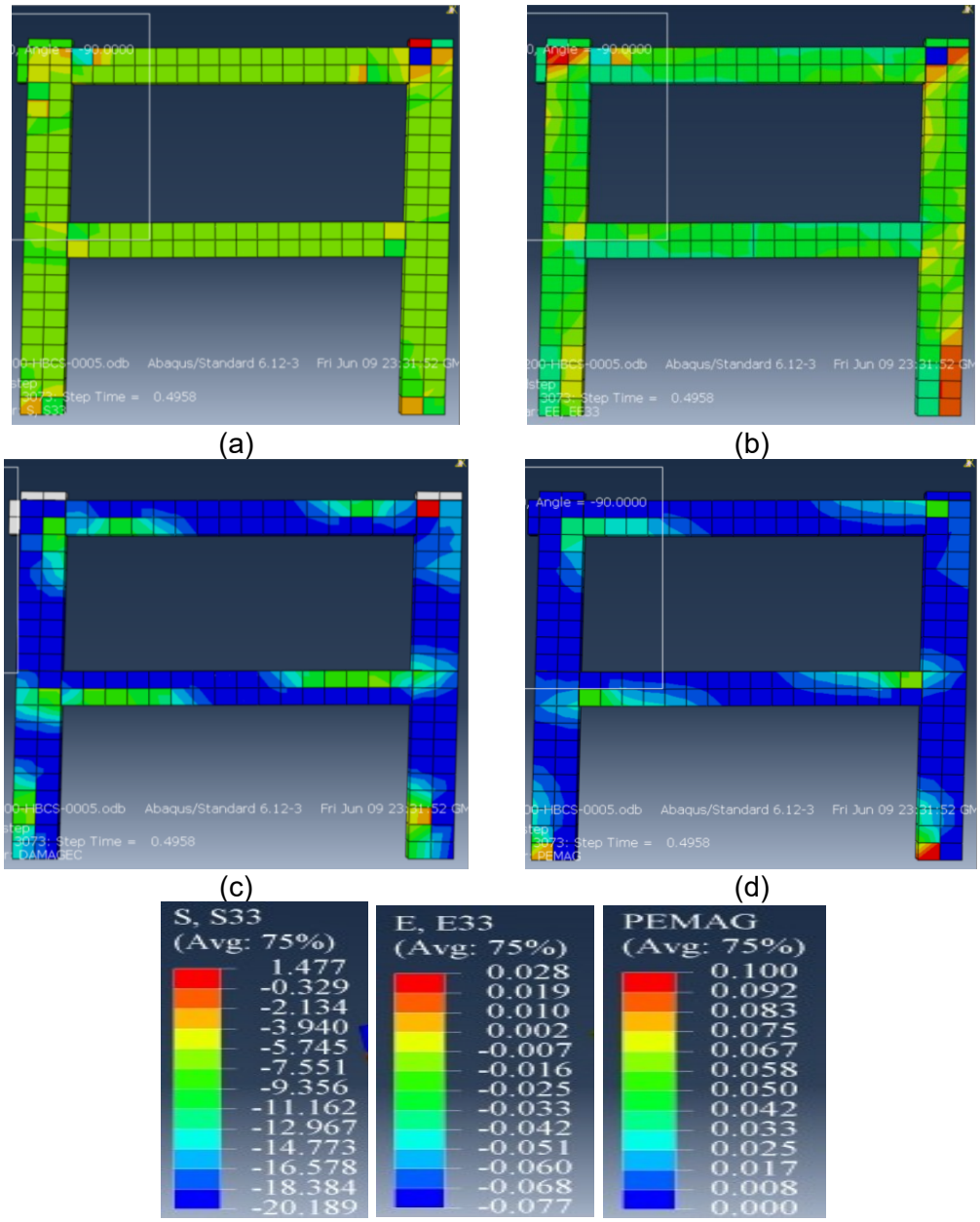


**Fig. 31**. HDBC (a) Stress S33, (b) Strain E33, (c) DAMAGEC, and (d) PEMAG at ULS (e) Values for S22, E33, and PEMAG

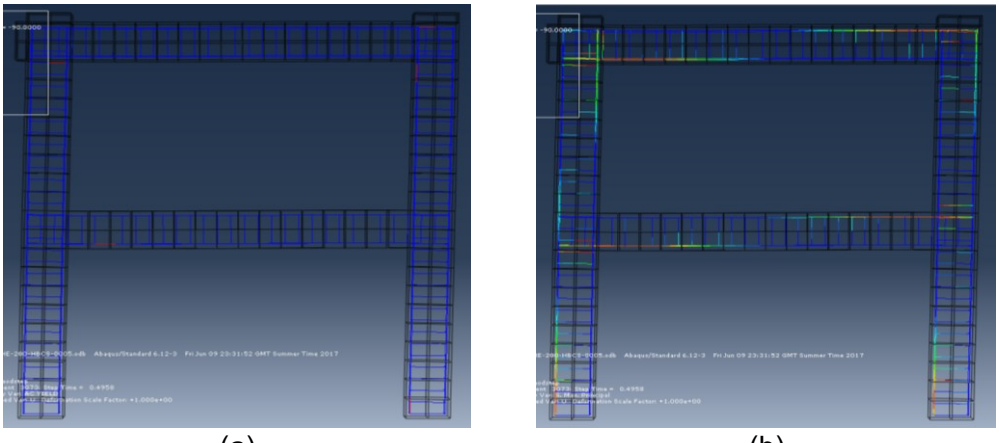


**Fig. 32**. HDBC (a) AC Yield and (b) Max Principal Stress at ULS (c) Values for AC YIELD and S, Max

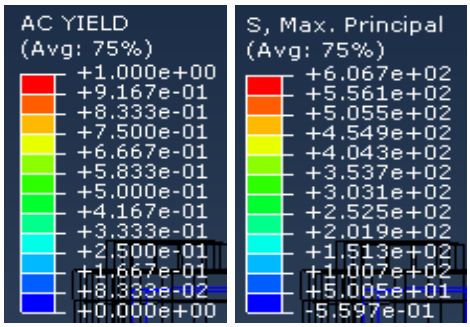


(c)

**Fig. 32**. (continued)

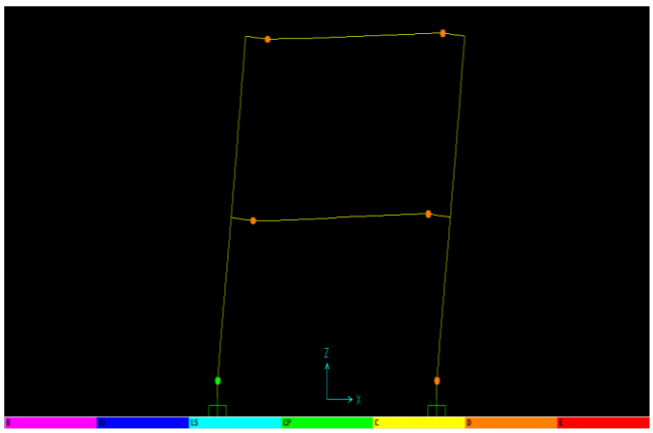

(a) SAP Result

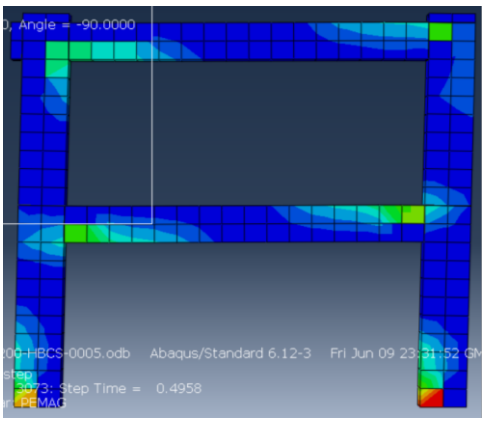


(b) ABAQUS Result

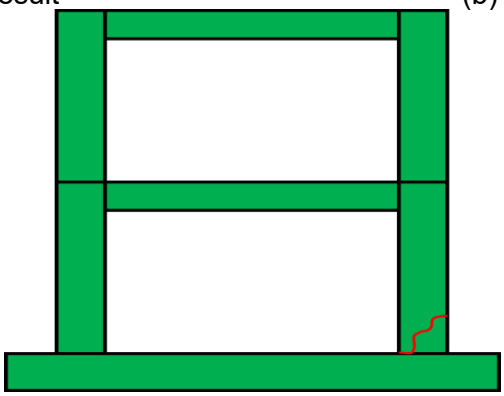

(c) ANN-FE Result

**Fig. 33**. Results (a) SAP 2000, (b) ABAQUS for HDBC, (c) ANN-FE

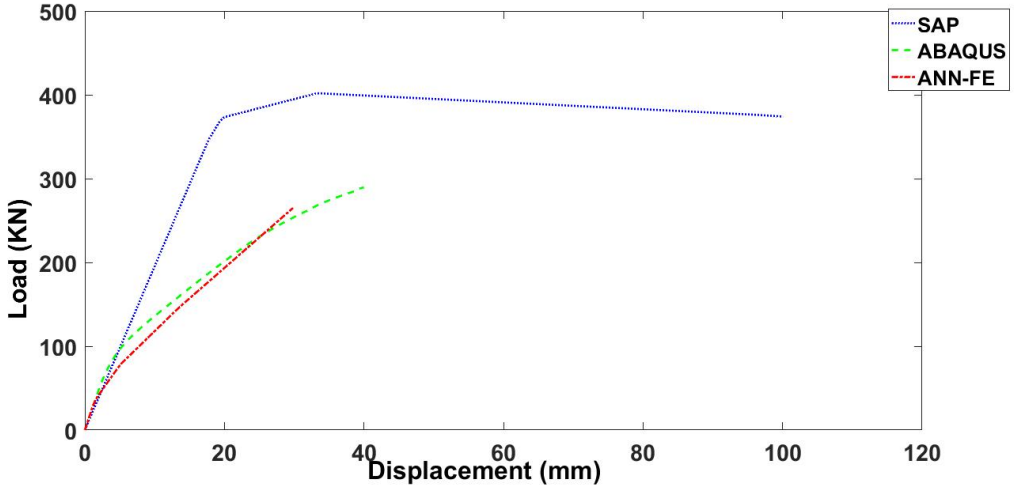


**Fig. 34**. Comparison of Load-Deflection curves obtained for HDBC

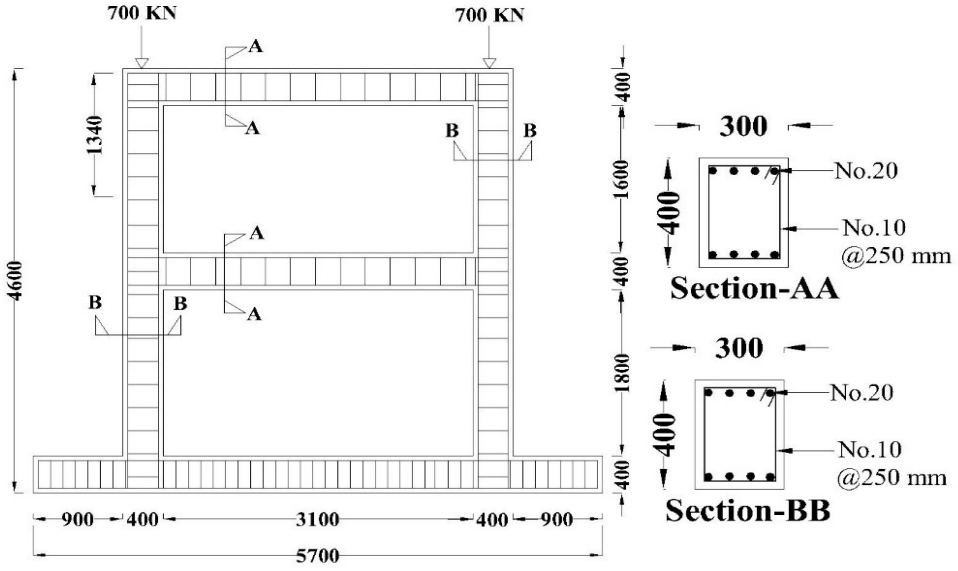


**Fig. 35**. Reinforcement details of DSBC

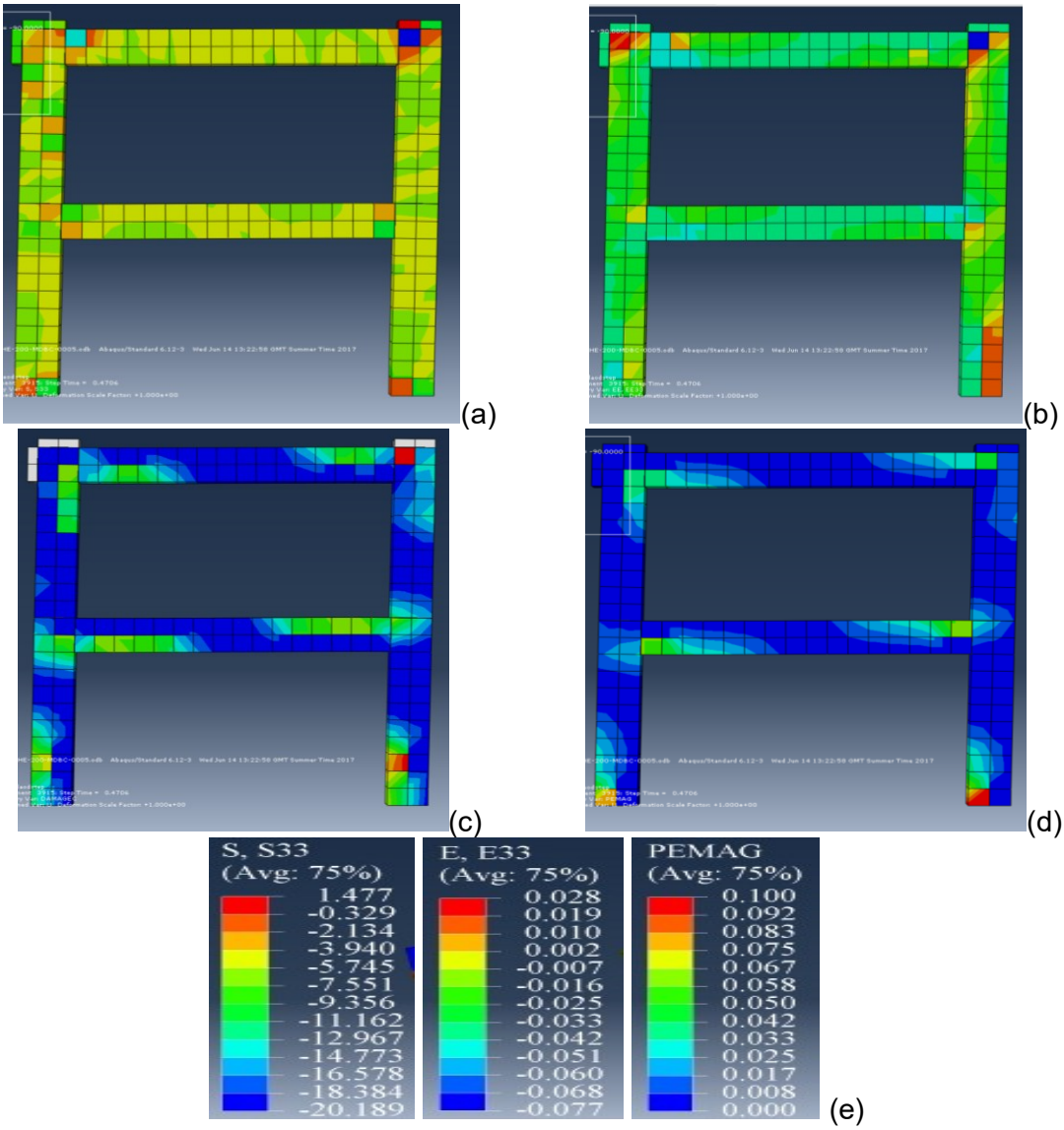


**Fig. 36**. DSBC (a) Stress S33, (b) Strain E33, (c) DAMAGEC and (d) PEMAG at ULS (e) Values for S22, E33 and PEMA

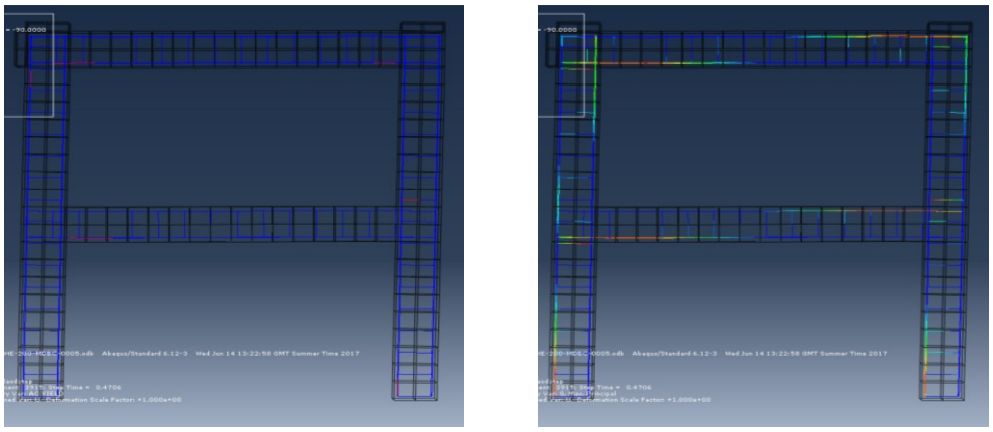

(a) (b)

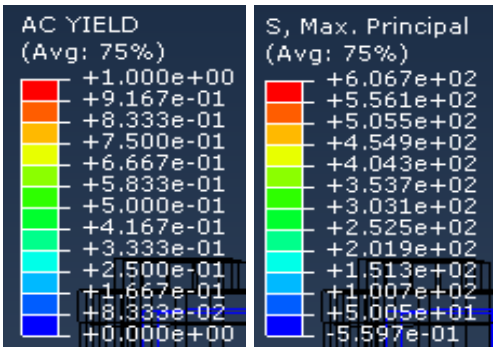


(c)

**Fig. 37**. DSBC (a) AC Yield and (b) Max Principal Stress at ULS (c) Values for AC YIELD and S, Max

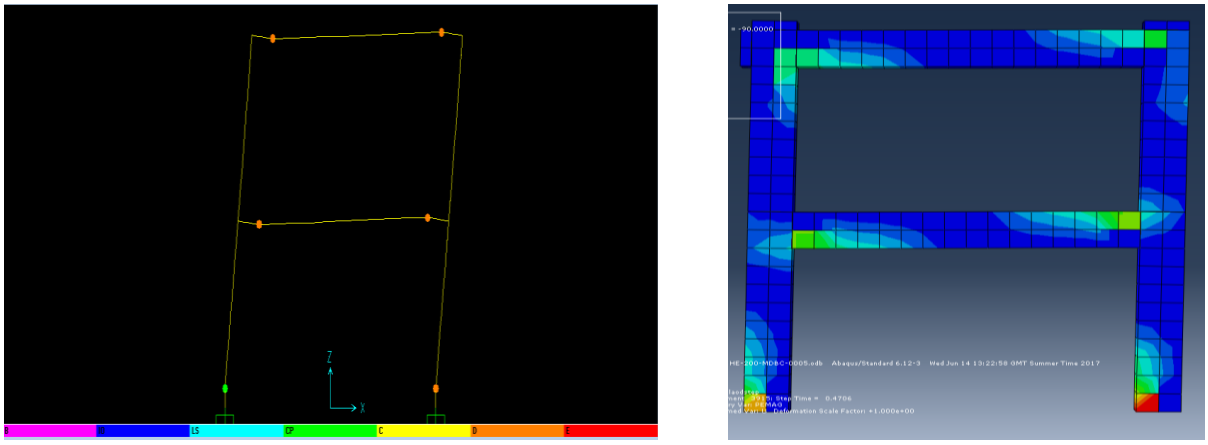

(a) SAP Result (b) ABAQUS Result

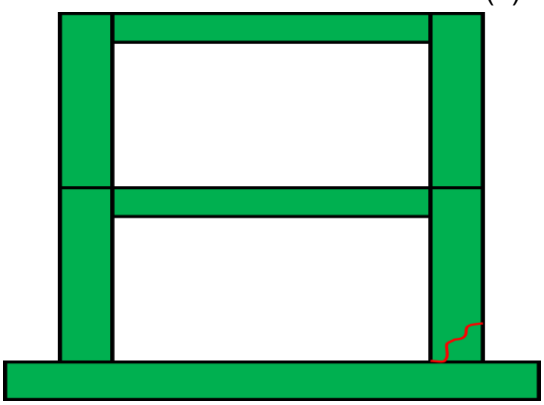

(c) ANN-FE Result

**Fig. 38**. Results of (a) SAP 2000, (b) ABAQUS for DSBC, (c) ANN - FE

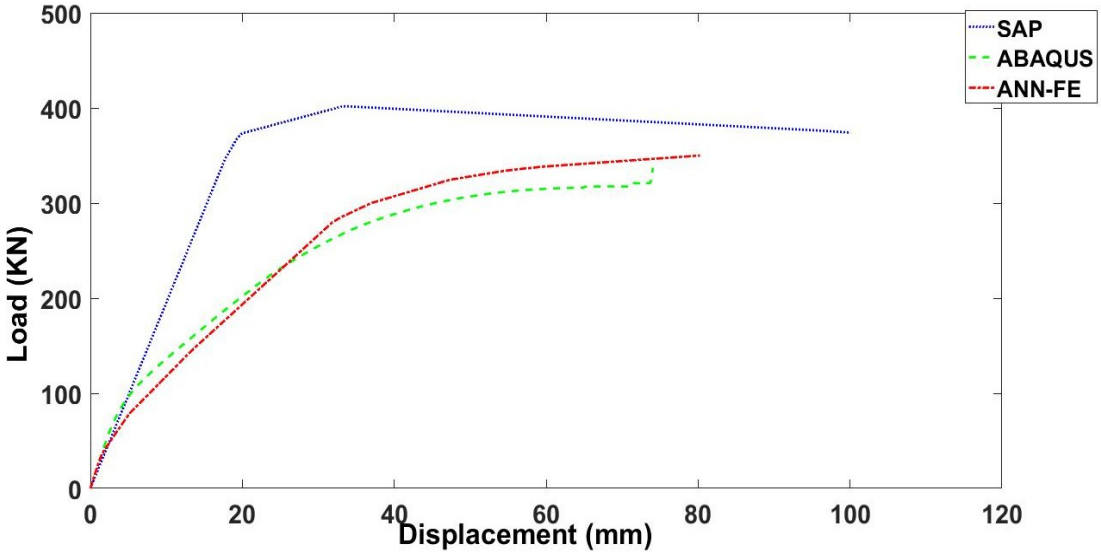


**Fig. 39**. Comparison of Load-Deflection curves for DSBC

**Table 8.** Analysis Time for the case of DSSB RC Frame EF

| Sr. No | Tools | Analysis Time of EF Models |
|---|---|---|
| 1 | SAP 2000 | 10 Minutes |
| 2 | ABAQUS | 15 Hours (Half Model) |
| 3 | ANN-FE | 25 Minutes (Python) |

Fig. 36 illustrates the structural response of the DSBC model at the ULS, showing contours of vertical stress (S33), strain (E33), compressive damage (DAMAGEC), and plastic strain (PEMAG).

Fig. 37 The ABAQUS FEA results for the HDBC model's reinforcement at the ULS are presented, showing the Axial Yield Criterion (AC Yield) and Maximum Principal Stress (S, Max) distributions to illustrate its stress and yield behavior.

Fig. 38 and Fig. 39 present a comparative analysis between experimental findings and numerical predictions generated using SAP2000, ABAQUS, and the proposed ANN-FEA approach for the DSBC-SF. Fig. 38 (a) shows the results from a pushover analysis conducted in SAP2000, highlighting the location and type of plastic hinges at the ULS. Fig. 38 (b) depicts the damage severity and distribution predicted by ABAQUS, and Fig. 38 (c) displays the crack pattern forecasted by the ANN-FEA model. The results showed that ANN-FEA exhibits similar failure to ABAQUS. However, SAP2000 exhibited different results.

Fig. 39 compares the structural response in terms of load versus displacement as predicted by three computational methods: SAP2000, ABAQUS, and ANN-FE. Initially, all approaches show a linear trend, representing elastic deformation. The SAP2000 model extends further in displacement and maintains load capacity up to around 50 mm, indicating a more ductile or extended response. In contrast, both the ABAQUS and ANN-FE models terminate at a displacement of approximately 20 mm, suggesting that their simulations were either constrained or reflected an earlier peak behavior. The ANN-FE method predicts a slightly higher load than ABAQUS for the same range, pointing to differences in model interpretation or data learning behavior. This divergence among models highlights the varying levels of conservatism and accuracy in capturing material or structural performance under increasing deformation.

Beyond predictive accuracy, computational efficiency is a critical advantage of the proposed ANN-FEA method. As shown in Table 8, the analysis time required by the ANN-FE tool is comparable to a SAP 2000 push-over analysis and

only 2.27% of the time needed by ABAQUS.

### 7.4. Comparative study between FEM models

The Fig. 40 illustrates the comparison of lateral displacements by encompassing (i) experimental results, (ii) ABAQUS [8], (iii) SAP-2000 [11] and (iv) ANN-FEA, for the four case studies mentioned above, i.e., (a) CM, (b) HDB, (c) HDBC, and (d) DSBC. The experimental results are only available for the CM configuration, showing a lateral displacement of approximately 60 mm, whereas no experimental data is reported for HDB, HDBC, and DSBC.

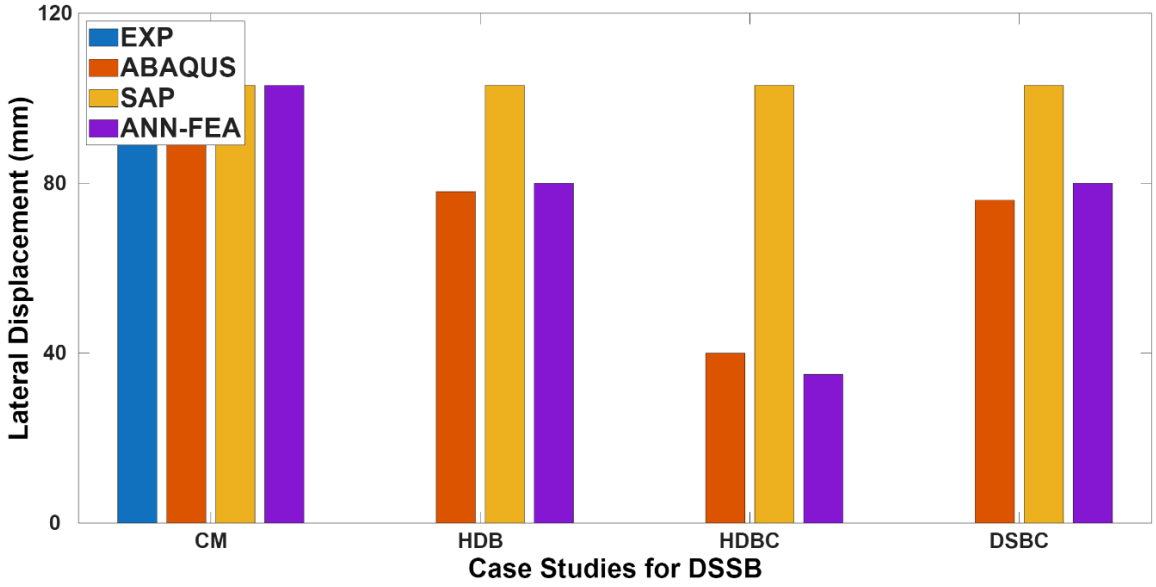


**Fig. 40**. Lateral displacement comparison of all models

In the numerical simulations, ABAQUS and ANN-FEA demonstrate a variation in lateral displacements among the configurations, with the CM model exhibiting the highest displacement 30 mm and other configurations (HDB, HDBC, DSBC) showing progressively lower values. This variability suggests that ABAQUS is sensitive to the material properties and boundary conditions employed in the modelling. In contrast, the SAP simulation results display uniform lateral displacements of 90 mm across all configurations, indicating the potential insensitivity of the SAP model to material-specific variations or possible oversimplifications in the modelling assumptions. Notably, the experimental displacement for the CM configuration is significantly higher than the corresponding values predicted by both ABAQUS [8] and SAP2000 [11]. This discrepancy highlights potential challenges in capturing real-world structural behavior within numerical simulations, such as the influence of imperfections, nonlinear material behavior, or boundary conditions that may not be adequately modeled. In summary, while the numerical tools provide valuable insights, the uniformity in SAP-2000 results and the divergence from experimental data necessitate further refinement in modeling approaches. Additionally, conducting experimental validation for all configurations is essential to enhance the reliability of the findings and establish a more robust correlation between experimental and simulation outcomes.

The Fig. 41 illustrates the comparison of lateral load by encompassing (i) experimental results, (ii) ABAQUS [8], (iii) SAP-2000 [11] Sand (iv) ANN-FEA, for the four case studies mentioned above, i.e., (a) CM, (b) HDB, (c) HDBC, and (d) DSBC. In the experimental results, only the CM configuration is represented, showing a lateral load of approximately 60 kN. The absence of experimental data for the HDB, HDBC, and DSBC configurations limits the ability to validate the numerical simulation results comprehensively. For the numerical simulations, ABAQUS and ANN-FEA demonstrate variation in lateral load capacity among the configurations. The HDB configuration

exhibits the highest load, closely followed by the CM configuration, while the HDBC and DSBC configurations show slightly lower lateral load values. This variation indicates ABAQUS's sensitivity to the material properties and boundary conditions applied in the models. Conversely, the SAP-2000 results reveal uniform lateral loads 90 kN across all configurations. This uniformity suggests that the SAP-2000 model may not adequately capture material-specific differences or boundary condition variations, potentially due to oversimplified assumptions or a lack of sensitivity in its modeling framework.

The discrepancy between the experimental load for the CM configuration and the numerical predictions from both ABAQUS, ANN-FEA, and SAP-2000 highlights potential limitations in the simulation models, such as an inability to fully replicate real-world conditions, including imperfections, nonlinearities, or other influential factors. In conclusion, while the numerical simulations provide valuable insights into structural performance, the consistent results from SAP and the lack of experimental data for specific configurations highlight the need for experimental validation across all configurations. Furthermore, enhancing the modelling strategies in numerical tools could improve their predictive accuracy, bridging the gap between simulated and experimental outcomes.

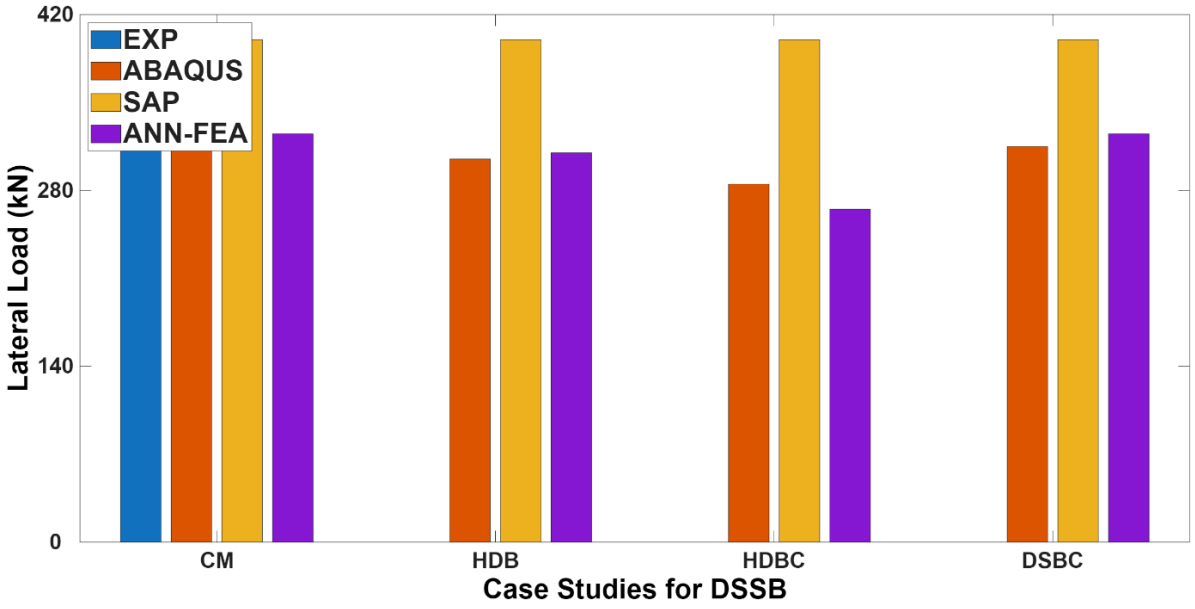


**Fig. 41**. Lateral Load Comparison of all models

## 8. Numerical modeling details

For the SAP2000 analysis, the model employs default concentrated plastic hinges at member ends using automatic hinge properties based on FEMA 356/ASCE 41 provisions. The hinge definitions include both flexural (M3) hinges for beams and axial-moment interaction (P-M2-M3) hinges for columns. However, the default configuration does not include explicit shear hinges, which may explain the different displacement ranges observed in the pushover curves compared to ANN-FEA and ABAQUS.

The ABAQUS model utilizes the Concrete Damaged Plasticity (CDP) material model with the following key parameters: dilation angle of 38 degrees, eccentricity of 0.1, biaxial-to-uniaxial compressive stress ratio ($f_{b0}/f_{c0}$) of 1.16, and Kc of 0.667. The mesh consists of C3D8R solid elements for concrete with an approximate size of 25mm, while reinforcement is modeled using embedded T3D2 truss elements. Boundary conditions include fixed supports at column bases with displacement control applied at the beam-column joint level. The comparison basis for all models is the peak base shear capacity at the Ultimate Limit State (ULS), with curves terminated when member capacity is

reached.

**9. Limitations**

This study has several limitations that should be acknowledged: (1) The ANN models are trained on databases with specific parameter ranges (as shown in Tables 1 and 2), and predictions outside these ranges should be treated with caution; (2) Experimental validation is limited to the CM configuration, while findings for parametric variants (HDB, HDBC, DSBC) are based on numerical comparisons; (3) The ANN-FEA stopping criterion corresponds to ULS capacity cutoff and does not simulate post-peak softening behavior; (4) The current implementation focuses on static pushover analysis and has not been validated for dynamic or cyclic loading scenarios; and (5) The member-level ANN models assume specific support conditions that may differ from actual frame boundary conditions under different loading scenarios.

**10. Discussion and conclusion**

The analysis of four cases demonstrates that the finite element models (FEM) effectively replicate the behavior of reinforced concrete (RC) frames with various detailing approaches. The findings of this investigation lead to several key conclusions:

1. The incorporation of shear effects is critical for the safe and accurate evaluation of the strength and ductility of RC frames, particularly for essential frames that are prevalent in practice.

2. Numerical simulations performed using ABAQUS exhibit sensitivity to material properties and boundary conditions, whereas the results from SAP indicate a degree of uniformity across configurations, suggesting potential oversimplifications. It is imperative to refine numerical modeling techniques and include material-specific variations to enhance predictive accuracy and bridge the disparity between experimental and simulated outcomes.

3. A comparison of experimental and numerical results reveals significant discrepancies, especially with the CM configuration. This finding highlights the limitations of numerical models in accurately replicating real-world structural behavior. Additionally, the absence of experimental data for the HDB, HDBC, and DSBC configurations underscores the necessity for comprehensive experimental validation to bolster the reliability of numerical simulations.

4. The comparative analysis of the finite element models indicates substantial variations in lateral load capacity relative to the CM configuration. The findings confirm that all newly developed finite element analysis (FEA) models demonstrate lower lateral load capacities: -4.45%, -13.8%, and -5.2% for the HDB, HDBC, and DSBC configurations, respectively. These discrepancies emphasize the sensitivity of structural responses to variations in reinforcement detailing and spacing configurations.

These observations raise significant concerns regarding the underlying assumptions employed in current assessment methods for RC structures. They point to an urgent need for the development of more sophisticated design and evaluation tools that accurately capture the behavior of RC structures under complex loading conditions, including high temperatures, fire, impact, blast, and environmental factors. Furthermore, these results underscore the necessity of reassessing the principles and assumptions of existing RC design codes to ensure their reliability and relevance in contemporary structural engineering practices.

**Funding:** This research received no external funding.

**Conflicts of Interest:** The authors declare no conflict of interest.

**Author Contributions:** AA: Idea, Paper writing analysis, investigation

**Ethics Approval and Consent to Participate:** Not applicable

**Data Availability and Replication of Results:** The data supporting this study's findings are available from the corresponding author upon reasonable request.

**References**

[1] D. Theodossopoulos, B. Sinha. (2013). A review of analytical methods in the current design processes and assessment of performance of masonry structures. *Construction and Building Materials*, 41, 990–1001. https://doi.org/10.1016/j.conbuildmat.2012.07.095

[2] W.J. Nordell. (1965). Plastic hinge formation in reinforced concrete beams. Naval Civil Engineering Laboratory, Port Hueneme, California, USA.

[3] H. Krawinkler, G.D.P.K. Seneviratna. (1998). Pros and cons of a pushover analysis of seismic performance evaluation. *Engineering Structures*, 20(4–6), 452–464. https://doi.org/10.1016/S0141-0296(97)00092-8

[4] A. Kadid, A. Boumrkik. (2008). Pushover analysis of reinforced concrete frame structures. *Asian Journal of Civil Engineering (Building and Housing)*, 9(1), 75–83.

[5] Y.C. Sung, T.K. Lin, C.C. Hsiao, M.C. Lai. (2013). Pushover analysis of reinforced concrete frames considering shear failure at beam-column joints. *Earthquake Engineering and Engineering Vibration*, 12(3), 373–383. https://doi.org/10.1007/s11803-013-0179-8

[6] S. Guner, F.J. Vecchio. (2010). Pushover analysis of shear-critical frames: Verification and application. *ACI Structural Journal*, 107(1), 72–81. https://doi.org/10.14359/51663390

[7] A. Sharma, G.R. Reddy, K.K. Vaze, R. Eligehausen. (2013). Pushover experiment and analysis of a full-scale non-seismically detailed RC structure. *Engineering Structures*, 46, 218–233. https://doi.org/10.1016/j.engstruct.2012.08.006

[8] Abaqus. (2012). Abaqus 6.12 documentation. SIMULIA, Dassault Systèmes, Providence, RI, USA.

[9] ADINA. (2015). ADINA system 9.2 documentation, Vol. 9.2. R&D, Inc., Watertown, MA, USA.

[10] ATHENA. (2005). ATHENA user's manual. SILVACO International, Santa Clara, CA, USA.

[11] Computers and Structures Inc. (2013). SAP2000. Berkeley, CA, USA.

[12] ACI. (2014). Building code requirements for structural concrete (ACI 318-14) and commentary. American Concrete Institute.

[13] EC2. (2004). Eurocode 2: Design of concrete structures – Part 1-1. European Committee for Standardization.

[14] JSCE. (2007). Standard specifications for concrete structures. Japan Society of Civil Engineers.

[15] NZS. (2006). Concrete structures standard NZS 3101. New Zealand Standards.

[16] KBCS. (2005). Korean Building Code – Structural. Architectural Institute of Korea.

[17] CSA. (2004). Design of concrete structures (CSA A23.3-04). Canadian Standards Association.

[18] M. Zakaria, T. Ueda, Z. Wu, L. Meng. (2009). Experimental investigation on shear cracking behavior in reinforced concrete beams with shear reinforcement. *Journal of Advanced Concrete Technology*, 7(1), 79–96. https://doi.org/10.3151/jact.7.79

[19] T. Stratford, C. Burgoyne. (2003). Shear analysis of concrete with brittle reinforcement. *Journal of Composites for Construction*, 7(4), 323–330. https://doi.org/10.1061/(ASCE)1090-0268(2003)7:4(323)

[20] S.R. Birgisson. (2011). Shear resistance of reinforced concrete beams without stirrups.

[21] G. Russo, D. Mitri, M. Pauletta. (2013). Shear strength design formula for RC beams with stirrups. *Engineering Structures*, 51, 226–235. https://doi.org/10.1016/j.engstruct.2013.01.024

[22] G. Campione, A. Monaco, G. Minafò. (2014). Shear strength of high-strength concrete beams: Modeling and design recommendations. *Engineering Structures*, 69, 116–122. https://doi.org/10.1016/j.engstruct.2014.02.029

[23] B. Bresler, A.C. Scordelis. (1963). Shear

strength of reinforced concrete beams. *Journal of the American Concrete Institute*, 60(4), 51–74.

[24] A. Marí, J. Bairán, A. Cladera, E. Oller, C. Ribas. (2015). Shear-flexural strength mechanical model for the design and assessment of reinforced concrete beams. *Structure and Infrastructure Engineering,* 11(11), 1399–1419. https://doi.org/10.1080/15732479.2014.964735

[25] M.D. Kotsovos. (2014). Compressive force-path method. Unified ultimate limit-state design of concrete structures. *Springer, Cham*. https://doi.org/10.1007/978-3-319-00488-4

[26] H.M. Günaydın, S.Z. Doğan. (2004). A neural network approach for early cost estimation of structural systems of buildings. *International Journal of Project Management,* 22(7), 595–602. https://doi.org/10.1016/j.ijproman.2004.04.002

[27] B. Shuraim. (2014). A novel approach for evaluating the concrete shear strength in reinforced concrete beams. *Latin American Journal of Solids and Structures*, 11, 93–112. https://doi.org/10.1590/S1679-78252014000100006

[28] M. Naser, G. Abu-Lebdeh, R. Hawileh. (2012). Analysis of RC T-beams strengthened with CFRP plates under fire loading using ANN. *Construction and Building Materials*, 37, 301–309. https://doi.org/10.1016/j.conbuildmat.2012.07.001

[29] M.A. Mashrei, R. Seracino, M.S. Rahman. (2013). Application of artificial neural networks to predict the bond strength of FRP-to-concrete joints. *Construction and Building Materials,* 40, 812–821. https://doi.org/10.1016/j.conbuildmat.2012.11.109

[30] C.A. Jeyasehar, K. Sumangala. (2006). Damage assessment of prestressed concrete beams using artificial neural network (ANN) approach. *Computers & Structures,* 84(26–27), 1709–1718. https://doi.org/10.1016/j.compstruc.2006.03.005

[31] N. Bakhary, H. Hao, A.J. Deeks. (2007). Damage detection using artificial neural network with consideration of uncertainties. *Engineering Structures,* 29(11), 2806–2815. https://doi.org/10.1016/j.engstruct.2007.01.013

[32] M.H. Arslan. (2012). Estimation of curvature and displacement ductility in reinforced concrete buildings. *KSCE Journal of Civil Engineering,* 16(5), 759–770. https://doi.org/10.1007/s12205-012-0958-1

[33] A.S. Genikomsou, M.A. Polak. (2015). Finite element analysis of punching shear of concrete slabs using damaged plasticity model in ABAQUS. *Engineering Structures*, 98, 38–48. https://doi.org/10.1016/j.engstruct.2015.04.016

[34] C.-B. Yun, J.-H. Yi, E.Y. Bahng. (2001). Joint damage assessment of framed structures using a neural networks technique. *Engineering Structures,* 23(5), 425–435 https://doi.org/10.1016/S0141-0296(00)00067-5

[35] S. Chakraborty, P. Kumar, S.K. Chakraborty. (2012). Neural network approach to response of buildings due to earthquake excitation. *International Journal of Geosciences,* 3(3), 630–639. https://doi.org/10.4236/ijg.2012.33063

[36] Z. Tadesse, K.A. Patel, S. Chaudhary, A.K. Nagpal. (2012). Neural networks for prediction of deflection in composite bridges. *Journal of Constructional Steel Research*, 68(1), 138–149.https://doi.org/10.1016/j.jcsr.2011.08.003

[37] S. Manoharan, S. Sathappan. (2012). A comparison and analysis of soft computing techniques for content-based image retrieval system. *International Journal of Computer Applications*, 59(13), 13-18.https://doi.org/10.5120/9607-4238

[38] A. Choudhary. (2014). A review of various soft computing techniques in the domain of

handwriting recognition. *International Journal of Information & Computation Technology*, 4(6), 601–606.

[39] N. Kandil, R. Wamkeue, M. Saad, S. Georges. (2006). An efficient approach for short-term load forecasting using artificial neural networks. *International Journal of Electrical Power and Energy Systems*, 28(8), 525–530. https://doi.org/10.1016/j.ijepes.2006.02.014

[40] L. Yu, S. Wang, K.K. Lai. (2006). An integrated data preparation scheme for neural network data analysis. *IEEE Transactions on Knowledge and Data Engineering*, 18(2), 1–14. https://doi.org/10.1109/TKDE.2006.22

[41] T.L. Lee, D.S. Jeng. (2002). Application of artificial neural networks in tide forecasting. *Ocean Engineering*, 29(9), 1003–1022. https://doi.org/10.1016/S0029-8018(01)00068-3

[42] K. Li, J.-X. Peng. (2007). Neural input selection—A fast model-based approach. *Neurocomputing*, 70(4–6), 762–769. https://doi.org/10.1016/j.neucom.2006.10.011

[43] M.Y. Rafiq, G. Bugmann, D.J. Easterbrook. (2001). Neural network design for engineering applications. *Computers and Structures*, 79(17), 1541–1552. https://doi.org/10.1016/S0045-7949(01)00039-6

[44] S. Talatahari, V.P. Singh, A.H. Alavi, F. Kang. (2015). Soft computing methods in civil engineering. *The Scientific World Journal*, 2015, 605871. https://doi.org/10.1155/2015/605871

[45] S.K. Sehra, Y.S. Brar, N. Kaur. (2011). Soft computing techniques for software project effort estimation. *International Journal of Advanced Computer and Mathematical Sciences*, 2(3), 160–167.

[46] L.A. Zadeh. (1998). Some reflections on soft computing, granular computing and their roles in intelligent systems. *Soft Computing*, 2(1), 23–25. https://doi.org/10.1007/s005000050030

[47] M.I. Waris, V. Plevris, J. Mir, N. Chairman, A. Ahmad. (2022). An alternative approach for measuring the mechanical properties of hybrid concrete through image processing and machine learning. *Construction and Building Materials*, 328, 126899. https://doi.org/10.1016/j.conbuildmat.2022.126899

[48] J. Mehmood, A. Ahmad, J.S. Cruz. (2022). Application of machine learning to predict the flexural moment capacity of near surface mounted beam. *1st International Conference on Advances in Civil & Environmental Engineering, University of Engineering & Technology Taxila, Pakistan.*

[49] W. Qayyum, R. Ehtisham, C.V. Camp, J. Mir, A. Ahmad. (2022). Detecting cracks with convolution neural network (CNN) with variable image dataset. *Proceedings of the 2nd International Conference on Recent Advances in Civil Engineering and Disaster Management.*

[50] M.F. Tahir, Q.U.Z. Khan, A. Ahmad. (2014). Effect of concrete strength on behavior of strip confined columns. *Technical Journal, University of Engineering and Technology Taxila*, 19(II-2014), 28-34.

[51] W. Qayyum, A. Aljuhni, N. Chairman, A. Ahmad. (2022). Evaluation of GoogLeNet, MobileNetV2, and InceptionV3 pre-trained convolutional neural networks for detection and classification of concrete crack images. *Proceedings of the 1st International Conference on Advances in Civil & Environmental Engineering (ACEE 2022), University of Engineering & Technology (UET) Taxila, Pakistan.*

[52] Q.U.Z. Khan, A. Ahmad, S. Mehboob, M. Nouman. (2020). Experimental and numerical investigation of T-joint enhanced confinement using flat steel strips. *Asian Journal of Civil Engineering,* 21, 1483–1492. https://doi.org/10.1007/s42107-020-00292-6

[53] W. Qayyum, R. Ehtisham, A. Bahrami, J. Mir, Q.U.Z. Khan, A. Ahmad, & Y.O. Özkılıç. (2023). Predicting characteristics of cracks in concrete

structure using convolutional neural network and image processing. *Frontiers in Materials*, 10, 1210543. https://doi.org/10.3389/fmats.2023.1210543

[54] M.H. Asad, S. Khaliq, M.H. Yousaf, M.O. Ullah, A. Ahmad. (2022). Pothole detection using deep learning. *Advances in Civil Engineering*, 2022, 9221211. https://doi.org/10.1155/2022/9221211

[55] A. Raza, Q.U.Z. Khan, A. Ahmad. (2020). Prediction of axial compressive strength for FRP-confined concrete members. *KSCE Journal of Civil Engineering*, 24(7), 2099–2109. https://doi.org/10.1007/s12205-020-1682-x

[56] G.M. Kotsovos, N.S. Zygouris. (2019). RC frame analysis with mode of failure prediction capability. *Magazine of Concrete Research,* 71(3), 109-125. https://doi.org/10.1680/jmacr.17.00092

[57] A. Ahmad. (2018). Reinforced concrete structures analysis and assessment with artificial neural networks. *Doctoral Theses. Heriot-Watt University. School of Energy, Geoscience, Infrastructure and Society (EGIS).*

[58] A. Ahmad, N.D. Lagaros, D.M. Cotsovos. (2021). Neural network-based prediction of reinforced concrete members. *Applied Sciences*, 11(11), 4975. https://doi.org/10.3390/app11114975

[59] A. Ahmad, D.M. Cotsovos. (2023). Reliability analysis of models for predicting T-beam response. *Proceedings of the ICE – Structures and Buildings*, 176(1), 28–50. https://doi.org/10.1680/jstbu.20.00129

[60] A. Ahmad, M.U. Arshid, T. Mahmood, N. Ahmad, A. Waheed, S.S. Safdar. (2021). Knowledge-based prediction of load-carrying capacity of RC flat slab through neural network and FEM. *Mathematical Problems in Engineering,* 4528945 https://doi.org/10.1155/2021/4528945

[61] A. Ahmad, D.M. Cotsovos. (2023). Reliability Analysis of RC Code for Predicting Load-Carrying Capacity of RCC Walls Through ANN. *Artificial Intelligence and Machine Learning Techniques for Civil Engineering. IGI Global Scientific Publishing, pp. 216–246*. https://doi.org/10.4018/978-1-6684-5643-9.ch009

[62] A. Ahmad, D.M. Cotsovos, N.D. Lagaros. (2020). Framework for the development of artificial neural networks for predicting the load carrying capacity of RC members. *SN Applied Sciences*, 2(4), 545. https://doi.org/10.1007/s42452-020-2353-8

[63] A. Ahmad, M. Elchalakani, N. Elmesalami, A. El Refai, F. Abed. (2021). Reliability analysis of strength models for short concrete columns with FRP rebars. *Journal of Building Engineering*, 42, 102497. https://doi.org/10.1016/j.jobe.2021.102497

[64] A. Ahmad, G. Kotsovou, D.M. Cotsovos, N.D. Lagaros. (2018). Assessing the accuracy of RC design code predictions using ANN. *International Journal of Advanced Structural Engineering*, 10(4), 349–365. https://doi.org/10.1007/s40091-018-0202-4

[65] F.J. Vecchio, M.B. Emara. (1992). Shear deformations in reinforced concrete frames. *ACI Structural Journal*, 89(1), 46–56. https://doi.org/10.14359/1283

[66] S. Sapna, A. Tamilarasi, M.P. Kumar. (2012). Backpropagation learning algorithm based on Levenberg–Marquardt algorithm. https://doi.org/10.5121/csit.2012.2438

[67] K. Gopalakrishnan. (2010). Effect of training algorithms on neural networks aided pavement diagnosis. *International Journal of Engineering Science and Technology*, 2(2), 83–92. https://doi.org/10.4314/ijest.v2i2.59147

[68] H. Yu, B.M. Wilamowski. (2011). Levenberg–Marquardt training. *Intelligent Systems*.

[69] M. Naeej, M. Bali, M.R. Naeej, J.V. Amiri. (2013). Prediction of lateral confinement coefficient in reinforced concrete columns using M5′ machine learning method. *KSCE Journal of Civil Engineering,* 17(7), 1714–1719. https://doi.org/10.1007/s12205-013-0214-3

[70] A. Ahmad, V. Plevris, Q.-U.-Z. Khan. (2020). Prediction of properties of FRP-confined concrete cylinders based on artificial neural networks. *Crystals,* 10(9), 811.https://doi.org/10.3390/cryst10090811

[71] D. Anderson, G. McNeill. (1992). Artificial neural networks technology. *Kaman Sciences Corporation.*

[72] Y. LeCun, L. Bottou, G.B. Orr, K.-R. Müller. (2002). Efficient BackProp. *Neural Networks: Tricks of the Trade. Springer, Berlin, Heidelberg*. https://doi.org/10.1007/3-540-49430-8_2

[73] K. De Jong, L. Fogel, H.-P. Schwefel. (1997). Handbook of Evolutionary Computation. *IOP Publishing*.

[74] H. Adeli. (2001). Neural networks in civil engineering: 1989–2000. *Computer-Aided Civil and Infrastructure Engineering*, 16(2), 126–142. https://doi.org/10.1111/0885-9507.00219

[75] R. Rojas. (1996). The Backpropagation Algorithm. *Neural Networks. Springer, Berlin, Heidelberg.* https://doi.org/10.1007/978-3-642-61068-4_7

[76] MathWorks. (2022). MATLAB. MathWorks.

[77] H.Z. Saeed, Q.U.Z. Khan, A. Ahmed, S.M. Ali, M. Iqbal. (2015). Experimental and finite element investigation of strengthened LSC bridge piers. *Composite Structures*, 131, 556–564. https://doi.org/10.1016/j.compstruct.2015.06.013

[78] A. Ahmad, A. Bahrami, O. Alajarmeh, N. Chairman, M. Yaqub. (2023). Investigation of circular hollow concrete columns reinforced with GFRP bars. *Buildings*, 13(4), 1056. https://doi.org/10.3390/buildings13041056

[79] A. Raza, Q.U.Z. Khan, A. Ahmad. (2021). Investigation of HFRC columns reinforced with GFRP bars. *Engineering Structures*, 227, 111461.https://doi.org/10.1016/j.engstruct.2020.111461

[80] A. Raza, Q.U.Z. Khan, A. Ahmad. (2019). Numerical investigation of GFRP-reinforced concrete members using CDP model. *Advances in Civil Engineering*, 2019, 1–21. https://doi.org/10.1155/2019/1745341

[81] A. Ahmad, Q.U.Z Khan, A. Raza. (2020). Reliability analysis of strength models for CFRP-confined concrete cylinders. *Composite Structures*, 244, 112312. https://doi.org/10.1016/j.compstruct.2020.112312

[82] Q.-U.-Z. Khan, M.F. Tahir, A. Ahmad, M. Iqbal. (2015). Seismic evaluation of repaired and retrofitted circular bridge piers. *Arabian Journal for Science and Engineering*, 40(11), 3057–3066. https://doi.org/10.1007/s13369-015-1769-8